The Astrophysical Journal, 743:90 (18pp), 2011 December 10 doi:10.1088/0004-637X/743/1/90

THE FIRST PUBLIC RELEASE OF SOUTH POLE TELESCOPE DATA: MAPS OF A 95 deg^2 FIELD FROM 2008 OBSERVATIONS

K. K. Schaffer[1,2,3], T. M. Crawford[1,4], K. A. Aird[5], B. A. Benson[1,2], L. E. Bleem[1,6], J. E. Carlstrom[1,2,4,6,7], C. L. Chang[1,2,7], H. M. Cho[8], A. T. Crites[1,4], T. de Haan[9], M. A. Dobbs[9], E. M. George[10], N. W. Halverson[11], G. P. Holder[9], W. L. Holzapfel[10], S. Hoover[1,6], J. D. Hrubes[5], M. Joy[12], R. Keisler[1,5], L. Knox[13], A. T. Lee[10,14], E. M. Leitch[1,4], M. Lueker[15], D. Luong-Van[5], J. J. McMahon[16], J. Mehl[1], S. S. Meyer[1,2,4,6], J. J. Mohr[17,18,19], T. E. Montroy[20], S. Padin[1,4,15], T. Plagge[1,4], C. Pryke[1,2,4,21], C. L. Reichardt[10], J. E. Ruhl[20], E. Shirokoff[10], H. G. Spieler[14], B. Stalder[22], Z. Staniszewski[15], A. A. Stark[22], K. Story[1,6], K. Vanderlinde[9], J. D. Vieira[15], and R. Williamson[1,4]

[1] Kavli Institute for Cosmological Physics, University of Chicago, 5640 South Ellis Avenue, Chicago, IL 60637, USA; kschaf2@saic.edu
[2] Enrico Fermi Institute, University of Chicago, 5640 South Ellis Avenue, Chicago, IL 60637, USA
[3] Liberal Arts Department, School of the Art Institute of Chicago, 112 S Michigan Ave, Chicago, IL 60603, USA
[4] Department of Astronomy and Astrophysics, University of Chicago, 5640 South Ellis Avenue, Chicago, IL 60637, USA
[5] University of Chicago, 5640 South Ellis Avenue, Chicago, IL 60637, USA
[6] Department of Physics, University of Chicago, 5640 South Ellis Avenue, Chicago, IL 60637, USA
[7] Argonne National Laboratory, 9700 S. Cass Avenue, Argonne, IL 60439, USA
[8] NIST Quantum Devices Group, 325 Broadway Mailcode 817.03, Boulder, CO 80305, USA
[9] Department of Physics, McGill University, 3600 Rue University, Montreal, Quebec H3A 2T8, Canada
[10] Department of Physics, University of California, Berkeley, CA 94720, USA
[11] Department of Astrophysical and Planetary Sciences and Department of Physics, University of Colorado, Boulder, CO 80309, USA
[12] Department of Space Science, VP62, NASA Marshall Space Flight Center, Huntsville, AL 35812, USA
[13] Department of Physics, University of California, One Shields Avenue, Davis, CA 95616, USA
[14] Physics Division, Lawrence Berkeley National Laboratory, Berkeley, CA 94720, USA
[15] California Institute of Technology, MS 249-17, 1216 E. California Blvd., Pasadena, CA 91125, USA
[16] Department of Physics, University of Michigan, 450 Church Street, Ann Arbor, MI 48109, USA
[17] Department of Physics, Ludwig-Maximilians-Universität, Scheinerstr. 1, 81679 München, Germany
[18] Excellence Cluster Universe, Boltzmannstr. 2, 85748 Garching, Germany
[19] Max-Planck-Institut für extraterrestrische Physik, Giessenbachstr. 85748 Garching, Germany
[20] Physics Department, Center for Education and Research in Cosmology and Astrophysics, Case Western Reserve University, Cleveland, OH 44106, USA
[21] Department of Physics, University of Minnesota, 116 Church Street S.E. Minneapolis, MN 55455, USA
[22] Harvard-Smithsonian Center for Astrophysics, 60 Garden Street, Cambridge, MA 02138, USA

Received 2011 July 28; accepted 2011 October 24; published 2011 November 23

ABSTRACT

The South Pole Telescope (SPT) has nearly completed a 2500 deg^2 survey of the southern sky in three frequency bands. Here, we present the first public release of SPT maps and associated data products. We present arcminute-resolution maps at 150 GHz and 220 GHz of an approximately 95 deg^2 field centered at R.A. 82.°7, decl. −55°. The field was observed to a depth of approximately 17 μK arcmin at 150 GHz and 41 μK arcmin at 220 GHz during the 2008 austral winter season. Two variations on map filtering and map projection are presented, one tailored for producing catalogs of galaxy clusters detected through their Sunyaev–Zel'dovich effect signature and one tailored for producing catalogs of emissive sources. We describe the data processing pipeline, and we present instrument response functions, filter transfer functions, and map noise properties. All data products described in this paper are available for download at http://pole.uchicago.edu/public/data/maps/ra5h30dec-55 and from the NASA Legacy Archive for Microwave Background Data Analysis server. This is the first step in the eventual release of data from the full 2500 deg^2 SPT survey.

Key words: cosmic background radiation – cosmology: observations – methods: data analysis – surveys

Online-only material: color figures

1. INTRODUCTION

1.1. Signals in the Millimeter-wave Sky

Millimeter-wavelength (mm-wave) maps of the sky contain rich cosmological and astrophysical information. Away from the Galactic plane, the mm-wave sky is dominated by the cosmic microwave background (CMB) at large and intermediate angular size scales. The CMB features on scales of roughly 5 arcmin to many degrees primarily arise from temperature fluctuations at the surface of last scattering, and mm-wave measurements of these anisotropies have enabled powerful constraints on cosmological models (e.g., Komatsu et al. 2011; Dunkley et al. 2011; Keisler et al. 2011). Interactions of CMB photons with matter can induce secondary anisotropies through processes such as gravitational lensing and scattering, and measurements of these additional anisotropies are potentially powerful probes of cosmic structure. The CMB features on scales smaller than about 5 arcmin are dominated by secondary anisotropy due to the inverse Compton scattering of CMB photons by free electrons, known as the Sunyaev–Zel'dovich (SZ) effect (Sunyaev & Zel'dovich 1972). On these small scales, emissive extragalactic sources also contribute significantly to the mm-wave sky. These sources are of considerable astrophysical and cosmological interest themselves, particularly the population of high-redshift, dusty, star-forming galaxies (DSFGs) that make up the bulk of the cosmic infrared background (CIB; Lagache et al. 2005). The current generation of mm-wave telescopes is just beginning to exploit the scientific potential of these small-scale signals.

The SZ effect consists of two components: the kinetic SZ (kSZ) effect and the thermal SZ (tSZ) effect. The kSZ effect is due to Doppler shifting of CMB photons by the bulk velocity of electrons along the line of sight. The tSZ effect is due to the scattering of CMB photons by hot, thermally distributed electrons, primarily in galaxy clusters. This interaction results in a spectral distortion of the CMB with a null at approximately 220 GHz. At observing frequencies above this null, the tSZ effect produces an increment in measured CMB flux, while at frequencies below the null, it produces a decrement. The resulting tSZ features in the mm-wave sky can be used to detect and characterize massive galaxy clusters. Galaxy clusters trace the largest peaks in the matter density field of the universe, and their abundance as a function of mass and redshift is a sensitive probe of structure growth. Galaxy clusters selected in a fine-angular-scale tSZ survey provide a nearly mass-limited and nearly redshift-independent sample for constraining cosmological parameters such as the dark energy equation of state parameter w and the normalization of the matter power spectrum σ_8 (e.g., Carlstrom et al. 2002). Such constraints are already being realized with just the first small fraction of data from large mm-wave surveys (Vanderlinde et al. 2010; Sehgal et al. 2010).

Measurements of the tSZ power spectrum provide additional cosmological constraints, independent of those from the primary CMB and from catalogs of individually detected clusters (Lueker et al. 2010; Dunkley et al. 2011; Shirokoff et al. 2011). These measurements can also inform models of the physical processes in galaxy clusters (e.g., Shaw et al. 2010; Battaglia et al. 2010). Measurements of the kSZ power spectrum are sensitive to, among other processes, the reionization history of the universe (e.g., Zahn et al. 2005), and limits on kSZ from mm-wave measurements have already ruled out some reionization scenarios (Mortonson & Hu 2010).

Two populations of extragalactic sources contribute most significantly to the mm-wave sky away from the Galactic plane: sources for which the flux decreases or is roughly constant with frequency, consistent with synchrotron emission from active galactic nuclei (AGNs); and sources for which the flux increases with frequency, consistent with thermal emission from DSFGs. Since the discovery by the SCUBA instrument (Holland et al. 1999) of a population of moderate-to-high-redshift DSFGs responsible for a significant fraction of the total CIB emission, DSFGs have been an active area of mm-wave and submillimeter (sub-mm) research. The recent discovery of a subpopulation of strongly lensed, higher-redshift DSFGs (Vieira et al. 2010; Negrello et al. 2010) has further increased interest in these sources. Measurements of synchrotron-emitting sources in mm-wave bands have the potential to constrain models of AGN physics (e.g., De Zotti et al. 2010).

1.2. The South Pole Telescope and Survey

The South Pole Telescope (SPT) is a 10 m telescope designed to survey a large area of the sky at mm and sub-mm wavelengths with arcminute angular resolution and low noise (Ruhl et al. 2004; Padin et al. 2008; Carlstrom et al. 2011). The current SPT receiver is a three-band (95, 150, and 220 GHz) bolometer camera optimized for studying the CMB and the tSZ effect. Since the SPT was commissioned in 2007, the majority of observing time has been spent on a survey of 2500 deg^2 designated the SPT–SZ survey. The final data set from the SPT–SZ survey will consist of maps for 19 contiguous subfields of 70–230 deg^2, observed during the austral winter seasons of 2008 through 2011. The final depth for most of the survey will be approximately 42, 18, and 85 μK arcmin[23] at 95, 150, and 220 GHz, with roughly 200 deg^2 (including the field discussed in this work) having deeper 220 GHz data. Following completion of the SPT–SZ survey, the receiver will be reconfigured for polarization sensitivity and will image a subset of the SPT–SZ survey area to significantly lower noise levels.

While three-frequency data from the complete 2500 deg^2 survey will eventually be released, the first public map release from the SPT–SZ survey consists of data taken during the 2008 season, when the SPT receiver was primarily sensitive in the 150 and 220 GHz bands. This first release presents maps covering approximately 95 deg^2 observed in those two bands. The area covered by these maps is referred to as the ra5h30dec-55 field, named for the J2000 coordinates of the approximate field center. This was the first large field mapped to survey depth by the SPT and was centered on a 45 deg^2 subregion optically surveyed by the Blanco Cosmology Survey[24] (BCS; S. Desai et al. 2011, in preparation). The BCS data were collected before the SPT was deployed, in anticipation of using the combination of optical and mm-wave data for joint galaxy cluster analyses. The center of the BCS region, and hence the center of the ra5h30dec-55 field, is R.A. 82.°7, decl. −55.°0. The ra5h30dec-55 field has been studied in detail to extract power spectrum measurements (Lueker et al. 2010; Hall et al. 2010; Shirokoff et al. 2011; Keisler et al. 2011) and to produce catalogs of emissive sources (Vieira et al. 2010) and SZ-selected galaxy clusters (Staniszewski et al. 2009; Vanderlinde et al. 2010; Williamson et al. 2011).

This paper presents the 2008 SPT maps of the ra5h30dec-55 field at 150 GHz and 220 GHz, discussing in detail the aspects of the instrument response and data processing that are relevant for interpreting and using the maps. We present maps with two variations in filtering and map projection, one designed for cluster finding and one designed for the detection and characterization of emissive sources. It is not possible to summarize all relevant features of the maps in a simple set of data products without some loss of information, which limits the use of these maps for certain types of analysis. In particular, the data products presented here are not sufficient to produce an extremely accurate noise model, nor to perform a cross-spectrum analysis for estimating the CMB power spectrum, nor to perform jackknife analyses to test for contamination (e.g., Shirokoff et al. 2011; Keisler et al. 2011). All of these would require all maps of individual observations of the ra5h30dec-55 field, which is an order-of-magnitude larger set of data products than what we are currently releasing. Individual-observation maps may be included in future releases.

Regardless of the intended use of the maps, we emphasize the importance of understanding how the SPT instrument response, data processing, map-making, and noise properties affect the signals of interest. To that end, after describing the instrument and observing strategy in Sections 2 and 3, we focus the majority of the paper (Sections 4 and 5) on a detailed discussion of these properties of the data. The maps themselves are presented in Section 6, which also presents cross-checks of analyses using these maps compared to previously published SPT analyses. Section 7 describes the data products available online. We

[23] Throughout this work, map signal and noise amplitudes are expressed in units of K-CMB, expressing deviations from the average measured intensity as equivalent temperature fluctuations in the CMB.

[24] http://cosmology.illinois.edu/BCS

provide an example calculation using these data products in the Appendix.

2. INSTRUMENT

The SPT is a 10 m off-axis Gregorian telescope located at the National Science Foundation's Amundsen–Scott South Pole Station, where atmospheric conditions are among the best in the world for mm and sub-mm observations (e.g., Radford 2011). The receiver images the sky using an array of transition-edge-sensor (TES) bolometers readout using frequency-multiplexed Superconducting QUantum Interference Device (SQUID) amplifiers. A description of the instrument design and performance can be found in Carlstrom et al. (2011). Here, we summarize the aspects of the instrument design and performance that are most relevant for understanding the data products in this release.

The detector array in the SPT–SZ receiver is made up of six wedge-shaped sub-arrays, each of which has 140 detector pixels configured to observe in one of the 95 GHz, 150 GHz, or 220 GHz observing bands.[25] These three observing bands have been selected to coincide with "windows" of high atmospheric transmission, and to optimize discrimination of the tSZ spectral signature. The observing bands are defined on the low-frequency end by a circular waveguide coupled to each detector, and on the high-frequency end by low-pass metal-mesh filters mounted above each detector wedge (Ade et al. 2006). Detectors across a given wedge have similar bandpass profiles, with an average bandwidth of 35 GHz for the 150 GHz band and 44 GHz for the 220 GHz band in the 2008 receiver. Details on the measured bands for 2008 are given in Section 4.1 and discussed further in L. E. Bleem et al. (2011, in preparation).

Data from each individual bolometer channel are digitized at 1 kHz, then digitally low-pass filtered and down-sampled to 100 Hz before being written to disk. We refer to the resulting data stream as time-ordered data (TOD). The optical time response of each detector is approximately described by a single-pole low-pass filter with time constants varying between 10 and 30 ms for different detectors. Measurements of the time response functions are presented in Section 4.2. The measured time response is deconvolved from the data during analysis, and additional anti-aliasing filters are applied when the data are binned to create maps, as described in Section 5.2.

Each detector's beam, defined as the response of the detector as a function of angle to a point source on the sky, is determined by the combination of a conical feedhorn above the detector and the optical design of the telescope (Padin et al. 2008). The main lobes of the beams are well described by two-dimensional Gaussians with average full widths at half-maximum (FWHM) of 1.15 and 1.05 arcmin at 150 GHz and 220 GHz, respectively. Individual detector beam profiles vary, primarily depending on their placement in the focal plane. However, a single average beam for each frequency is appropriate for characterizing the effective angular response in the final maps. Beam measurements are presented in Section 4.4.

Noise in the SPT–SZ data comes from four main sources: (1) noise due to statistical fluctuations in photon arrival time, (2) noise intrinsic to the detectors, (3) noise from the readout system, and (4) brightness temperature fluctuations in the atmosphere, mostly due to inhomogeneous mixing of water vapor. The first two components are expected to contribute essentially "white" noise (i.e., equal amplitude at all temporal frequencies). Readout noise has a white noise component as well as a "$1/f$" component, with power decreasing as temporal frequency increases. The spatial power spectrum of atmospheric fluctuations increases steeply with increasing spatial scale (e.g., Bussmann et al. 2005), leading to noise in the TOD that rises steeply at low temporal frequencies. The atmosphere dominates the SPT noise at frequencies below 1 Hz, while the photon noise dominates at the higher temporal frequencies that correspond to the signal region for cluster and point source science. Typical single-detector noise-equivalent-temperatures (NETs) expressed in CMB units range from approximately 380 to 540 μK$\sqrt{\text{s}}$ at 150 GHz and 640 to 850 μK$\sqrt{\text{s}}$ at 220 GHz for the data presented here. These NETs are estimated from the detector noise power spectra in a band corresponding to multipole $\ell \sim 3000$ in the scan direction, using the absolute temperature calibration described in Section 4.5.2 of this release. Given the typical numbers of detectors with good performance during 2008 observations, the total mapping speed was approximately 29 μK$\sqrt{\text{s}}$ at 150 GHz and 74 μK$\sqrt{\text{s}}$ at 220 GHz for the 2008 season.

3. OBSERVATIONS

The primary observing mode for the SPT is scanning across the sky at constant elevation. Because the SPT is located within 1 km of the geographic South Pole, this corresponds almost exactly to scans at constant declination. Complete observations of a field are assembled from many consecutive scans at stepped positions in elevation. Throughout each roughly 36 hr cryogenic cycle, we perform multiple short calibration measurements interleaved with the field observations. These calibration measurements include observations of a small chopped signal from a non-aperture-filling thermal source, two-degree scans in elevation, and observations of the Galactic H II regions RCW38 and MAT5a (NGC3576), which are common calibration sources for mm-wave CMB experiments (Puchalla et al. 2002; Coble et al. 2003; Kuo et al. 2007). This set of regular calibrations allows us to characterize instrument response and monitor detector performance, as described in Section 4.

Between February 13 and June 5 2008, 421 observations were performed of the ~95 deg^2 RA5H30DEC-55 field, each taking about 2 hr of observing time. Each complete observation comprised 176 constant-elevation scans across the field, with elevation offsets of $0\overset{\circ}{.}125$ between pairs of scans back and forth across the field. Twenty different initial starting elevations were used for successive observations, at offsets of $0\overset{\circ}{.}005$. Variations in the starting position of successive observations enhance the uniformity of coverage in combined maps. Approximately half of the observations of this field were performed with an azimuth scanning speed of 0.44 deg s^{-1}, with the remaining observations performed at 0.48 deg s^{-1}.

4. CHARACTERIZATION OF INSTRUMENT RESPONSE

4.1. Observing Bands

The SPT spectral bandpasses are measured using a beam-filling Fourier Transform Spectrometer (FTS), as described in L. E. Bleem et al. (2011, in preparation). Transmission spectra were measured for ~50% of the detectors on each of the six detector wedges. For a given wedge, the detector transmission spectra are highly uniform, with well-defined band edges at low and high frequencies that are set by a precision-machined circular waveguide and a common metal-mesh low-pass filter. For

[25] Each detector wedge has 161 potential bolometer channels, of which 140 are read out.

Table 1
SPT Average Band Properties

Property	150 GHz		220 GHz	
	Real	Delta-fn. Approx.	Real	Delta-fn. Approx.
Band center (GHz)	153.4	150	219.8	220
Bandwidth (GHz)	35.2	...	43.7	...
Conversion factors for power-law spectra				
Radio, $\alpha = -0.5$ (MJy sr^{-1} K^{-1})	396.3	398.6	476.7	483.7
Rayleigh-Jeans, $\alpha = 2$ (MJy sr^{-1} K^{-1})	389.6	398.6	487.7	483.7
Dusty, $\alpha = 3.5$ (MJy sr^{-1} K^{-1})	375.6	398.6	487.5	483.7
Effective f_{SZ}				
$T_e = 0$	−0.923	−0.954	0.006	0.038
$T_e = 8$ keV	−0.876	−0.903	−0.046	−0.018

detectors in the same wedge, the band center has an rms variation of ∼1%. For each band, we construct an average response by weighting each detector's transmission spectrum by the inverse square of the detector's NET. Uncertainties in the final spectra in each band are dominated by the absolute frequency calibration of the FTS. We can verify this by comparing the measured versus expected location of the low band edge (due to the circular waveguide cutoff), and we estimate this absolute frequency scale to be accurate to 0.3 GHz. The 150 and 220 GHz transmission spectra, averaged over all detectors in a given band, are available for download (see Section 7), expressed as the response to a beam-filling, flat-spectrum ($I(\nu) =$ constant) source, with the peak transmission normalized to unity.

In Table 1, we give the band center and effective bandwidth for the 150 and 220 GHz bands. We have defined the band center to be

$$\nu_{\rm cen} = \frac{\int \nu f(\nu)\, d\nu}{\int f(\nu)\, d\nu}, \tag{1}$$

where $f(\nu)$ is the transmission spectrum averaged over all detectors in a given observing band, and the effective bandwidth is defined to be $\int f(\nu)\, d\nu$.

To convert the SPT maps from CMB temperature units to intensity, one must consider both the spectrum of the source and the spectrum of the CMB. For a source with a spectrum $I(\nu) = I_0 S(\nu)$, this conversion factor is

$$\frac{I_0}{\Delta T} = \frac{\int A\Omega(\nu) \frac{dB}{dT}(\nu, T_{\rm CMB}) f(\nu)\, d\nu}{\int A\Omega(\nu) S(\nu) f(\nu)\, d\nu}, \tag{2}$$

where $A\Omega(\nu)$ is the telescope throughput, or etendue, and $(dB/dT)(\nu, T_{\rm CMB})$ is the differential change in brightness of the CMB for a change in temperature. For beam-filling sources in a single-mode system such as the SPT–SZ receiver, $A\Omega(\nu) = c^2/\nu^2$.

Spectra of astrophysical sources in mm-wave bands are typically approximated as power laws, such that $I(\nu) = I_0(\nu/\nu_0)^\alpha$. In Table 1, we give example conversion factors between CMB units and MJy sr^{-1} for beam-filling sources with α values typical of some common mm-wave source families. The conversion factors are quoted for ν_0 equal to the nominal band center, i.e., either 150 or 220 GHz. For comparison, we also quote the conversion factor that we would obtain if our bands were infinitely narrow and centered on the nominal band center. (The conversion factor in this case is simply $(dB/dT)(\nu, T_{\rm CMB}) \times 10^{20}$, reflecting the definition of 1 MJy $= 10^{-20}$ W m^{-2} Hz^{-1}.)

To convert a measured temperature fluctuation in a CMB map to an equivalent tSZ Comptonization or Compton-y parameter (e.g., Carlstrom et al. 2002), one simply divides the measured ΔT by the mean CMB temperature and a frequency-dependent tSZ factor. For delta-function bands, this factor is equal to

$$f_{\rm SZ}(\nu) = \left(x \frac{e^x + 1}{e^x - 1} - 4 \right) (1 + \delta_{\rm SZ}(x, T_e)), \tag{3}$$

where $x = h\nu/k_B T_{\rm CMB}$, $\delta_{\rm SZ}(x, T_e)$ is a small relativistic correction (e.g., Nozawa et al. 2000), and T_e is the electron temperature of the cluster. For SPT bands and a beam-filling source, the effective band-averaged $f_{\rm SZ}$ is equal to

$$\langle f_{\rm SZ} \rangle = \frac{\int \nu^{-2} f_{\rm SZ}(\nu) \frac{dB}{dT}(\nu, T_{\rm CMB}) f(\nu)\, d\nu}{\int \nu^{-2} \frac{dB}{dT}(\nu, T_{\rm CMB}) f(\nu)\, d\nu}. \tag{4}$$

In Table 1, we give values of effective, band-averaged $f_{\rm SZ}$ for two values of T_e (0 and 8 keV) for both the real bands and the delta-function approximations.

4.2. Detector Time Constants

The temporal response function of SPT detectors over the signal band of interest for this work ($\leqslant$10 Hz) can be described by a single-pole low-pass filter, with each detector characterized by a single time constant. The time constants are measured periodically using the chopped thermal calibrator. The time constants are estimated by fitting the amplitude and phase response of each detector using a sequence of chopper frequencies from 5 to 10 Hz. Time constants are verified using fast scans of the detectors across bright astrophysical sources. Maps constructed using only left-going scans can be subtracted from maps constructed with only right-going scans to verify that residual time constant errors do not contribute significant spurious signal in the combined maps. Exactly these tests were performed in CMB power spectrum analyses of SPT data including the RA5H30DEC-55 field (Lueker et al. 2010; Shirokoff et al. 2011; Keisler et al. 2011), and no spurious signal was found. The time constants do not change significantly over a season or with receiver temperature over the range of data used in the final maps, so for analysis purposes a single time constant parameter is associated with each detector for all observations during a given season. Time constants for the 2008 receiver configuration vary between about 10 and 30 ms across the detector array, with median values of 19 ms and 17 ms for 150 GHz and 220 GHz detectors, respectively.

4.3. Pointing Reconstruction and Astrometry

The real-time pointing model used to control the telescope is initially calibrated using optical star cameras mounted on the

telescope structure, as described in more detail in Carlstrom et al. (2011). The pointing reconstruction of the mm-wave data is then calculated offline using daily measurements of Galactic H II regions and information from thermal, linear displacement, and tilt sensors.

During each cryogenic cycle, full observations are performed of the H II regions RCW38 and MAT5a. For each of these observations, the response of each detector is fit to a scaled, translated version of a template image of the H II region. After any modification of the focal plane or optical configuration (typically once a year), a set of the RCW38 observations is used to measure each detector's pointing offset relative to the telescope boresight. The daily observations of both RCW38 and MAT5a throughout the observing season are used to constrain the pointing model over time, and the RCW38 measurements contribute to estimation of relative calibrations, as described in Section 4.5.1. After the pointing model has been corrected using the H II region and telescope sensor information, random errors in the pointing reconstruction of roughly 7″ rms remain from observation to observation. These random errors contribute to the width of the effective beam in the final co-added maps, as described in the following section.

The absolute astrometry of the final co-added maps was initially calibrated by comparing the SPT positions of a handful of sources to those sources' positions in the 843 MHz Sydney University Molongolo Sky Survey catalog (Mauch et al. 2003). This calibration was expected to be accurate at the 10″ level. The recent publication of the Australia Telescope 20 GHz Survey (AT20G) catalog (Murphy et al. 2010) provides an even more accurate astrometric calibration. The astrometry in the AT20G catalog is tied to Very Long Baseline Interferometry (VLBI) calibrators and is accurate at the 1″ level. Using 17 sources in the SPT 150 GHz data, we find very low scatter between SPT and AT20G positions. We do, however, see a small (<10″) but statistically significant mean offset from the AT20G positions. We correct this offset by simply changing the definition of the field center for the ra5h30dec-55 maps from its nominal value of R.A. 82.°70000, decl. −55.°00000 to R.A. 82.°70247, decl. −55.°00076. After this correction has been applied, the SPT positions of the 17 sources agree with the AT20G positions to better than 1″ in the mean, with arcsecond-level scatter. An estimated uncertainty of 2″ in each dimension accounts for statistical uncertainty in the SPT source detections and systematic uncertainties due to potential offsets in the source centers at the ATCA and SPT observing bands and potential offsets between the SPT 150 GHz and 220 GHz maps.

4.4. Beams

A thorough understanding of the detector beams, or angular response functions, is critical for interpreting the signals in SPT maps. Sky signals are convolved with these functions in the process of observation, leading to the extended appearance of point sources in the maps and the suppression of small-scale power in the angular power spectrum. The structure of the SPT beams can be characterized as a Gaussian main lobe out to a radius of 1 arcmin, near sidelobes at radii between 1 and 5 arcmin, and a diffuse, low-level sidelobe at radii between 5 and 40 arcmin relative to the beam center.

Dedicated observations of planets are valuable for measuring the far sidelobes, since planets are bright enough to adequately probe the tails of the response function. Planet observations are less useful for studying the main beam, however, because of the limited dynamic range of the detectors, and because the planets are extended sources. We use observations of the brightest quasar in each survey field to characterize the main beam shape. We reconstruct a two-dimensional profile of the beam by stitching together measurements of the "inner beam" within a 4 arcmin radius, and an "outer beam" covering radii from 4 arcmin to 40 arcmin.

The outer-beam measurements are based on seven dedicated observations of Venus performed in 2008 March, and one dedicated observation of Jupiter performed in 2008 August. The observations consisted of a sequence of azimuth scans with 0.5 arcmin elevation steps between scans. Because the detectors are saturated when they observe the planets directly (and require several detector time constants to recover), only data from the first half of each scan is used. For Jupiter observations, the impact of the Jovian satellites, which is very small to begin with, is mitigated by subtracting a template based on their known locations. The Venus and Jupiter data are filtered to remove atmospheric noise and CMB fluctuations, with the locations of the planets masked in the filtering. The average scan-synchronous signal, as measured at distances larger than 40 arcmin from the planet, is subtracted from the maps.

The inner beam shapes for this data release are measured using a bright quasar that appears in the ra5h30dec-55 field itself and a bright quasar that appears in the other field observed by SPT in 2008, the ra23h30dec-55 field. We have no evidence that the beam shape differs between these two fields. A small map is constructed around the brightest source in each field. The source is masked to a radius of 5 arcmin and filtering is applied to remove atmospheric noise and CMB. The residual CMB and noise in the central beam region leads to an approximately constant offset to the absolute response in this map. The inner beam profile based on the quasar map is then stitched together with the outer beam profile from Jupiter, with an iterative procedure that uses the Venus maps to determine the scaling between the two components and to correct for the constant offset in the inner maps.

This procedure leads to a composite two-dimensional beam profile that describes both the main beam and far-sidelobe response of the instrument. In addition, because the inner-beam measurement is based on the final co-added maps of the fields, it encapsulates the contribution of several-arcsecond random pointing variations to the effective angular response in the final maps. Pointing variations increase the effective beam width by approximately 3% and 5% at 150 GHz and 220 GHz, respectively.

The inner and outer beam profiles for both bands are presented in Figure 1. The composite beam maps are available for download, as described in Section 7.

In many applications, it is preferable to use a simplified approximation to the beam profiles rather than the full two-dimensional angular response functions. Azimuthally averaged beam functions in map space and Fourier space are presented in Figure 2. Using the flat-sky approximation, we calculate the Fourier transform (FT) of the composite beam map, $B(\ell, \phi_\ell)$. From this, we compute the azimuthally averaged beam function,

$$B_\ell = \sqrt{\frac{1}{2\pi}\int |B(\ell, \phi_\ell)|^2 \, d\phi_\ell}. \quad (5)$$

There is a small bias (<0.5% fractional error at $\ell < 10{,}000$) in this estimate of B_ℓ due to residual map noise and we remove this bias.

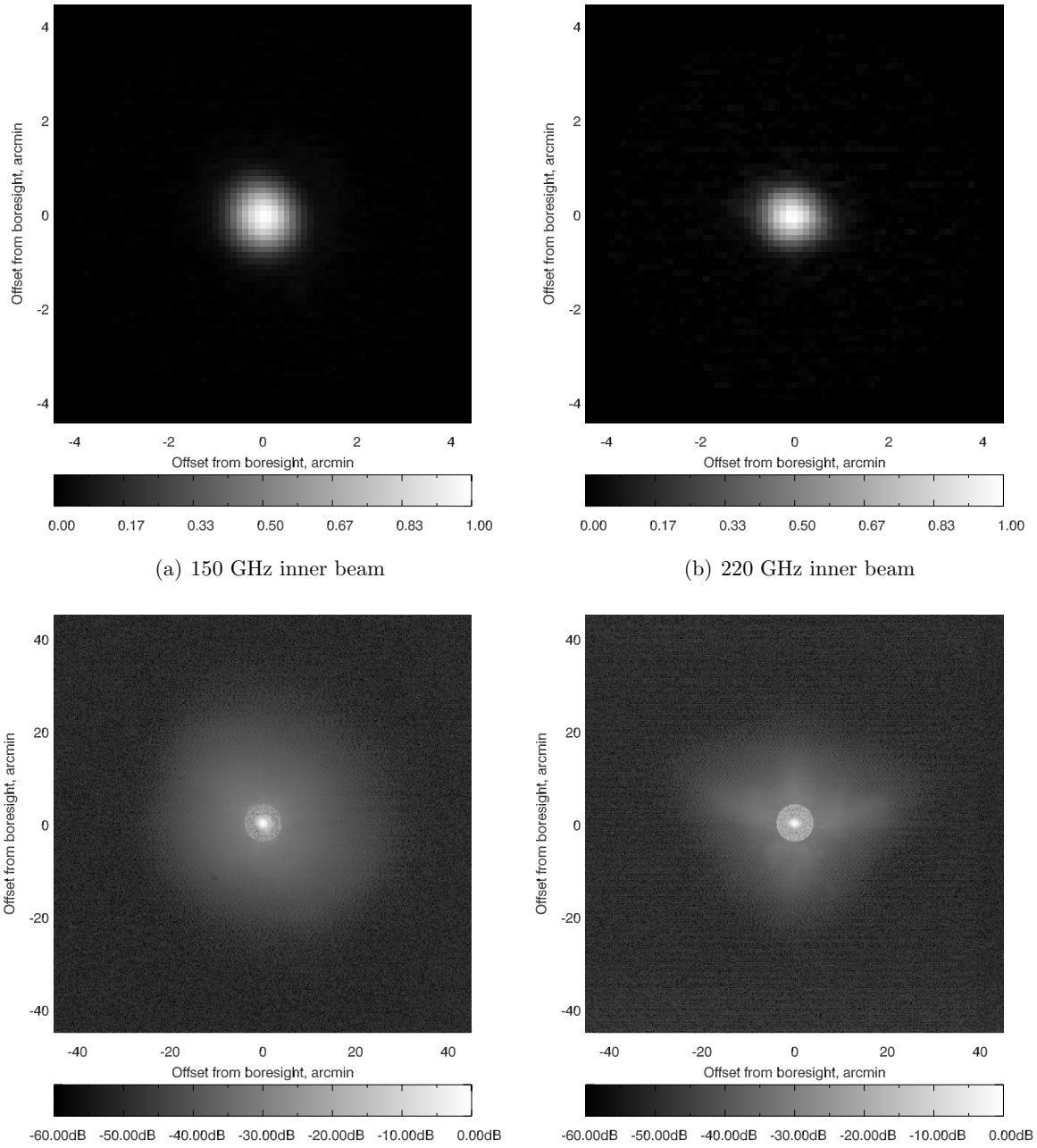

(a) 150 GHz inner beam (b) 220 GHz inner beam

(c) 150 GHz outer beam (d) 220 GHz outer beam

Figure 1. Two-dimensional average beam functions for the RA5H30DEC-55 field. Panels (a) and (b) show the 150 GHz and 220 GHz two-dimensional beam profiles on a linear scale, emphasizing the structure of the "inner beam." Panels (c) and (d) show the beam functions on a logarithmic scale out to much greater radii, emphasizing the structure of the "outer beam," and showing the stitching of the two beam estimates at a radius of 4 arcmin. Note that in panels (c) and (d) the absolute value has been taken in order to display the image on a logarithmic scale, but this visually exaggerates the appearance of the noise in the innermost 4 arcmin of the beam.

The normalization of $B(\ell)$ is somewhat arbitrary, in that it is degenerate with the absolute, CMB-power-spectrum-based calibration factor described in Section 4.5.2. Our CMB-power-spectrum-based calibration uses the multipole range $650 \leqslant \ell \leqslant 1000$, so we choose to normalize $B(\ell)$ to 1 at $\ell = 800$ to minimize the correlation between beam uncertainty and calibration uncertainty.

The uncertainty in our estimate of $B(\ell)$ arises from several statistical and systematic effects, including residual atmospheric noise in the maps of Venus and Jupiter, and the weak dependence of B_ℓ on the choice of radius used to stitch together the inner and outer beam maps. We consider seven sources of uncertainty in total. In Figure 2, we show the quadrature sum of these error estimates, which approximates the total uncertainty. The beam functions are uncertain at the few percent level, and this uncertainty increases mildly with increasing multipole number.

4.5. Calibration

Averaging measurements from many detectors within a given observation requires correcting for their relative gains. To average multiple single-observation maps together, we also need to correct for inter-observation detector gain variations and changes in atmospheric opacity that affect the calibration of the whole array. Section 4.5.1 describes our procedure for estimating detector-to-detector and day-to-day relative calibrations. When all of these relative calibration factors are applied, a

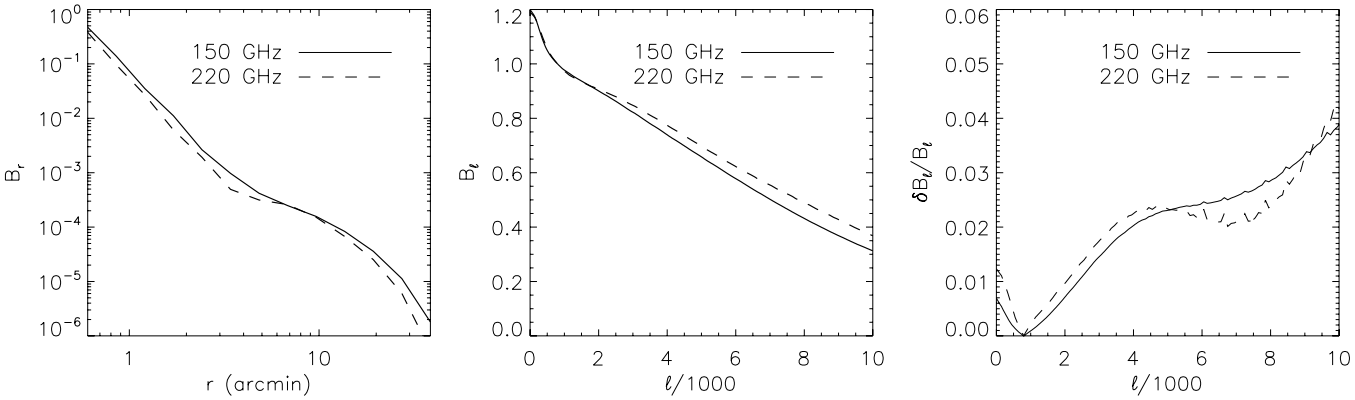

Figure 2. Azimuthally averaged beam profiles (left), Fourier-space beam functions (center), and fractional uncertainties (right).

single absolute calibration number relates the amplitudes in the final map to physical units. Section 4.5.2 describes our procedure for estimating the final absolute calibration for each map. The physical units chosen for our maps are K-CMB, expressing deviations from the average measured intensity as equivalent temperature fluctuations in the CMB.

4.5.1. Relative Gain Calibrations

Two types of calibration observation are combined to account for detector-to-detector relative gains, temporal gain variations, and atmospheric opacity variations: (1) daily observations of the H II region RCW38 and (2) observations of the chopped thermal calibration source that illuminates the focal plane from the center of the telescope secondary mirror. The thermal calibration source illuminates the focal plane through a small hole in the secondary mirror; hence, the effective source shape seen by the detectors is very different from that of sources on the sky and varies over the focal plane.

The thermal calibration source is observed many times per day, and we use these observations to correct for variations in response to sky signal across the array (flat fielding) and to correct for any gain drifts. The first step in the relative calibration pipeline is to relate each detector's response to the calibration source to its response to an astrophysical source. To do this, we assign an effective temperature to the calibration source for each detector, based on the season average of ratio between the response to the calibration source and the response to RCW38. The relative calibration for each detector over a single RA5H30DEC-55 observation is then based on the response to the calibration source observation nearest that field observation. To account for any day-to-day drifts in the calibration source filament temperature or illumination pattern, we correct the single-observation relative calibration number for each detector using the wedge-averaged difference between that observation's calibrator response and the season average. Similarly, to account for any changes in atmospheric opacity, we correct each detector's calibration using the wedge-averaged difference between response to the nearest RCW38 observation response and the season average. The relative calibration factors applied to a given detector are typically stable to within 2% over the season.

4.5.2. Absolute Calibration

The H II regions RCW38 and MAT5a can be used as absolute calibrators, but their irregular shapes and the uncertainties in their absolute fluxes at mm-wavelengths limit the precision of the calibration. An RCW38-based absolute calibration has been used for some previous work (Staniszewski et al. 2009; Williamson et al. 2011; Story et al. 2011), but here we adopt a refined absolute calibration based on comparisons of CMB angular power spectra produced from SPT and WMAP data. The two approaches give calibrations that are consistent within their uncertainties.

To calibrate the co-added maps to absolute temperature units, we estimate the angular power spectrum of the CMB at 150 GHz using the technique described in Keisler et al. (2011). The maps used in this estimation have been preliminarily calibrated using the RCW38-based calibration. The resulting spectrum is then compared to the well-calibrated WMAP7 power spectrum (Larson et al. 2011) over the multipole range $650 \leqslant \ell \leqslant 1000$, and the final calibration to apply to the 150 GHz SPT maps is determined by requiring the inverse-variance-weighted ratio of the SPT and WMAP7 power spectra to be unity over this range. To reduce the contribution of SPT noise and sample variance to the calibration uncertainty, we use all 2008 data to derive the calibration for the RA5H30DEC-55 field. We have looked for evidence of calibration differences between the 2008 data from the RA5H30DEC-55 field and the rest of that season's data by checking the regular observations of MAT5a, and we constrain this difference to be smaller than 1% in temperature. A cross-power spectrum is constructed using the 150 GHz and 220 GHz maps, correcting for differences in beams and filtering between the two bands. The ratio of this cross-power spectrum to the power spectrum at 150 GHz for multipoles dominated by primordial CMB signal gives an estimate of the relative calibration between the two bands, which is used to transfer the 150 GHz absolute calibration to 220 GHz.

We estimate that the uncertainty in our 150 GHz absolute temperature calibration is 3.1% using this calibration method. The uncertainty in the 220 GHz absolute calibration is estimated to be 6.9%. Note that since the 220 GHz calibration derives from the 150 GHz calibration, the two uncertainties are correlated with a correlation coefficient of approximately 0.5.

5. DATA PROCESSING AND MAP-MAKING

Raw TOD are processed into maps in two stages. In the first ("pre-processing") stage, the raw data from a single observation of the field are calibrated, data selection cuts are applied, and initial filtering and instrument characterization are performed. The same pre-processing pipeline is used for all SPT survey data, regardless of the intended final use of the maps, although there have been some minor modifications in the data selection

criteria and pre-processing algorithms over the history of SPT data analysis.

In the second ("map-making") stage, additional filtering is performed on the pre-processed TOD and the data are binned into single-observation maps used for final co-adds. The filtering applied in the map-making stage is typically customized for different analyses, as is the choice of map projection. As described in detail below, we present two specific combinations of filtering and map projection in this release.

We characterize the effect of the filtering and projection choices by describing the Fourier-space properties of the maps. We refer to features in the Fourier plane using the corresponding angular wavenumbers in radians **k**. The maps are oriented such that at the center of the map, the *x*-direction corresponds to R.A. and the *y*-direction corresponds to declination.

5.1. Data Selection and Pre-processing

The first steps in the pre-processing pipeline are to characterize detector performance, assemble measured response characteristics, and calculate calibration factors and weights.

Summary statistics are first calculated to characterize the receiver setup and the TOD for each detector. Each detector's TOD for an entire 2 hr observation is used to estimate the power spectral density (PSD) for that detector. A fit to the noise PSD is then used to identify line-like features that deviate from a $1/f$ plus white noise profile. Additional noise statistics are calculated for the SQUIDs.

Next, a set of responsivity statistics is assembled for every detector. These include the amplitude of the detector's response to the chopped thermal calibrator, the amplitude of its response during a calibration observation of RCW38, and the amplitude of its response to a two-degree elevation scan performed before each field observation. These response parameters are used to calculate daily gain calibrations for each detector, as previously described in Section 4.5. They are also used to define data selection cuts.

Preliminary cuts verify that each bolometer's bias voltage and readout configuration settings are within the nominal ranges and that the TOD values for each channel remain within the dynamic range of the digitizer. Once these initial cuts have been applied, bad bolometers are rejected with progressively more and more stringent assessments of responsivity and noise.

The first such cuts enforce a minimum signal-to-noise response to the chopped calibration source and a minimum response to the routine elevation scans. Bolometers are also rejected if their response to the elevation scans does not fit the expected modulation of the atmosphere. If a detector's response to the chopped calibration source or the short elevation scans is more than three standard deviations away from the median response for detectors of the same band, it is also rejected. Detectors are rejected if their PSDs exhibit wide line-like features or too many lines. After all of these cuts are applied, a final pair of cuts rejects bolometers with calibration constants or noise weights that deviate by more than a factor of three from the median for each band. The median numbers of detectors that pass cuts for the ra5h30dec-55 field observations (quoted in Section 5.6) reflect the bolometers selected through this process.

The bolometer data are parsed into scans, defined as temporally contiguous periods of constant-velocity azimuth scanning in either direction across the field. Cutting periods of time when the telescope is accelerating (at the ends of each scan) removes about 5% of the total TOD for an observation. All data for a given scan are cut if the receiver temperature exceeded the nominal operating value at any time during the scan, if the telescope following error (absolute value of the commanded position minus the position recorded by the encoders) exceeded 20″ at any time during the scan, or if there were data acquisition problems leading to bolometer data or pointing data drop-outs during the scan. Typically about 5% of scans are cut for these reasons. Data for an individual bolometer in an individual scan are also rejected if that bolometer shows evidence of step-function features in its TOD (which can sometimes occur due to "flux jumps" in the SQUIDs), if the SQUID or bolometer noise for that scan is excessive, or if any of the digitized SQUID data approach the limits of the dynamic range. A spike-finding algorithm identifies cosmic-ray-like events in the TODs for individual detectors. If there are fewer than five in a given scan, and the spike features are relatively small, we remove them and interpolate over the gaps; otherwise, we flag and ignore affected TODs for the duration of the scan. Typically, around 5% of otherwise well-performing bolometers are cut from each scan for any of these reasons.

Because a varying subset of detectors will sometimes show sensitivity to the receiver's pulse-tube cooler (a phenomenon also seen in other TES bolometer systems with pulse-tube coolers, e.g., Dicker et al. 2009), we apply a notch filter to remove a small amount of bandwidth from all data during the pre-processing stage. Combining all data that pass selection cuts for a given observation, we identify the fundamental frequency of the pulse-tube cooler and notch-filter a conservative 0.007 Hz of bandwidth around this frequency as well as any strong harmonics. For the 2008 ra5h30dec-55 field observations, the pulse tube operating frequency was 1.62 Hz. If all harmonics of this frequency were always cut, this would represent an absolute maximum of 0.4% of the total bandwidth; the actual bandwidth cut is smaller since typically only the first few harmonics are cut. We have verified that this notch filter has a negligible effect on further analysis, and we neglect it in further analysis steps.

After all pre-processing, the offline pointing model is used to calculate corrected pointing positions to associate with every time sample, and the pre-processed data are written into an intermediate data format for further analysis.

5.2. Filtering

After the pre-processing stage of data analysis, the TOD associated with a given field observation is further filtered on a scan-by-scan basis. The processing of each scan (1) deconvolves the detector temporal response functions, (2) removes high-frequency temporal noise that translates to spatial scales smaller than the pixel resolution in the maps, and (3) removes atmospheric noise while minimizing the filtering of signal power.

The time-constant deconvolution and low-pass anti-aliasing filters are applied in a single Fourier-domain operation on each scan for each detector. The time-constant deconvolution takes into account the measured time constants for every individual detector (see Section 4.2). A cutoff frequency of 25 Hz is used for the low-pass filter applied to the TOD, chosen to limit noise on spatial scales smaller than the 0.25 arcmin map pixels without suppressing power on the spatial scales of the SPT beams.

Prior to averaging the data into maps, additional time-domain filtering is applied to remove atmospheric noise. The atmospheric contamination resides primarily at low temporal frequencies, so a high-pass filter is an effective way to remove the most contaminated data. However, the application of a Fourier-domain high-pass filter will also distort the appearance of bright point sources in the final maps, introducing "ringing"

patterns. This effect can be avoided by filtering in the time domain via fitting to slowly varying template functions and masking the locations of known bright point sources during the fit. Point-source masking of this sort has been performed for one of the sets of maps in this release, but not for the other, as explained in Section 5.3.

In all variations of our analysis, we fit out a mean and slope as well as higher-order polynomials from each scan. In some past work we have subtracted Legendre polynomials and in others a series of sines and cosines (Fourier modes). In either case the result is a time-domain high-pass filter that allows for point-source masking as needed. For the maps in this release, we have fit Fourier modes up to a temporal frequency that corresponds to a spatial high-pass cutoff of $k = 300$ in the scan direction, or $k_x = 300$ (because the scan direction corresponds to the x-direction in our maps).

Atmospheric noise is highly correlated across the detector array. By taking this correlation into account, we can filter additional atmospheric noise without affecting small-scale sky signal. For each TOD sample, we subtract the mean value across every detector in a given wedge. This filter can also be performed with the locations of bright point sources masked, and this masking is performed in one set of maps in this release (as with the masking in the time-series filters).

5.3. Filtering Variations for Maps in This Release

This paper presents two sets of maps, one tailored to cluster analysis and one tailored to point-source analysis.[26] For cluster analysis, the point sources in the maps are viewed as a foreground. The locations of known point sources are masked in the filtering for these maps in order to prevent artifacts from ringing, which could affect cluster extraction. The brightest 201 sources are masked in the filtering, with the top 9 masked to a radius of 5 arcmin and the rest masked to 2 arcmin. The source list used for constructing the mask was created by merging together all sources detected at greater than 5σ significance in either 150 GHz or 220 GHz maps, from the published point-source catalog for this field (Vieira et al. 2010), and adding any sources that lie outside the field boundaries used for detection in that work but that are strongly detected in an analysis using all map pixels.

When the point sources themselves are the object of study, it is preferable to filter them in the same way as the other parts of the map, so that the effect of filtering on signal can be completely characterized. For the set of maps tailored to point-source analysis, the brightest point sources are not masked in the filtering. We also choose different map projections for the two sets of maps, as described below. All other parameters of the data processing and filtering are equivalent in both sets of maps.

5.4. Map Projections

After all data selection and filtering has been performed, we use the corrected pointing information to average and bin the data into pixels in a two-dimensional map. For small areas of the sky, analysis of the maps is greatly simplified by using a flat-sky approximation. This allows two-dimensional FTs to be used (rather than spherical harmonic transforms) for analyzing signal power, noise, and instrument response as a function of angular scale. However, any choice of map projection will lead to some distortions of information in the map. The character of these distortions varies depending on the selected projection, meaning that some analyses may be easier to perform on maps with one projection while others may be easier with another.

In past work we have employed several different projection schemes, of which two have been selected for presentation here. Past SPT cluster-finding analysis has used the Sanson-Flamsteed projection (e.g., Calabretta & Greisen 2002), which projects constant-elevation scans into pixel rows in the final map. This projection choice simplifies the characterization and treatment of signal filtering, because the TOD processing effectively operates on map rows. The disadvantage of this projection is that it is not distance preserving, and sky features near the corners of the maps will therefore have slightly distorted shapes (for example, a 1 arcmin circle will appear to have an ellipticity of $\epsilon \sim 0.12$ near the corner of the ra5h30dec-55 map). We have selected this projection for the maps tailored to cluster finding.

The second projection employed here, for the maps tailored to point-source analysis, is the oblique Lambert equal-area azimuthal projection. For the typical size, shape, and center location of SPT maps, this sky projection preserves both distances and areas to high accuracy (Snyder 1987), which means that the effective beam shape will not vary significantly for different locations in the map. This is particularly advantageous for reconstructing point-source amplitudes using variants of the CLEAN algorithm (Högbom 1974). The disadvantage of this projection is that the effective filtering has a strong position dependence, since the angle between the scan direction and the map pixel rows changes across the map. For constant-declination scans, this angle, α, can be expressed as

$$\alpha = \tan^{-1}(A/B), \tag{6}$$

where

$$A = \gamma \sin\theta_0 \sin(\phi_0 - \phi) \times (\sin\theta_0 \cos\theta + \sin\theta \cos\theta_0 \cos(\phi_0 - \phi)) + \cos\theta_0 \sin(\phi_0 - \phi),$$

$$B = \gamma \sin\theta_0 \sin^2(\phi_0 - \phi) \sin\theta + \cos(\phi_0 - \phi),$$

and

$$\gamma = \frac{0.5}{1 + \cos\theta_0 \cos\theta + \sin\theta_0 \sin\theta \cos(\phi_0 - \phi)}.$$

Here ϕ equals the R.A. in radians, while $\theta = \pi/2 -$ declination, also in radians. Unsubscripted variables represent the pixel location and the subscript "0" denotes the field center.

In Sections 6.2 and 6.3, we will discuss the impact of the choice of projection on the signal and noise properties in these maps.

5.5. Weights

The weights used to co-add data from many detectors into a single-observation map are calculated by averaging the calibrated PSD for each detector between 1 and 3 Hz. For the telescope scan speeds used in observations of the ra5h30dec-55 field, this frequency range corresponds to a multipole range of roughly $1500 < \ell < 4500$ in the scan direction, a reasonable overlap with the scales of interest for source and cluster detection and for high-ℓ power spectrum analyses.

[26] The majority of extragalactic emissive sources appear point like in the arcminute-resolution SPT maps, and we use "point source" and "emissive source" interchangeably in this work.

When we average the data from individual detectors to obtain a measurement of the map value in a particular pixel, we calculate the total weight for that pixel by combining the weights from each individual detector. These pixel weights are used to combine the multiple single-observation maps into a final co-added map (see Section 5.6). The primary source of noise variation between single-observation maps is the weather, which is accurately reflected in the calibrated 1–3 Hz noise estimates for the individual detectors in all but the poorest-weather days.

The weights for the final map are used to define the uniform-coverage region. We define the uniform-coverage region as the area of the resulting map at 150 GHz for which the weight in a map pixel exceeds 95% of the median for all map pixels, resulting in an approximate area of 95 deg^2.

5.6. Co-adding Single-observation Maps

If all single-observation maps of the RA5H30DEC-55 field in a given observing band were identical up to noise variations captured accurately by the pixel weights described in the previous section, then the final maps in each band would simply be weighted averages over all the single-observation maps. In reality, some fraction of single-observation maps need to be excluded from the final co-add based on anomalous behavior in the telescope, the weather, or the detectors.

Of the 421 total observations of the RA5H30DEC-55 field, we reject 55 from consideration for final maps because they were performed with atypical gain settings for the detectors or had pointing control problems leading to atypical coverage of the field. We reject an additional 21 observations that were incomplete, due to the need to cycle the cryogenic system.

We examine the weights and the noise rms in the central five-by-five-degree region of the individual observation maps and make further cuts based on the weight and noise rms statistics. We have found that two particular cuts are necessary to optimize the final map noise and avoid biased signal values in the final map. First, we cut any observations with anomalously high weights, a condition which implies that the recorded detector noise rms is lower than we can reasonably expect, possibly because changes in loading have significantly altered the detectors' operating point. We also cut individual maps in which the product of the median weight and the noise rms squared is anomalously high. This can occur if the total map rms on all scales does not track the 1–3 Hz noise on which the weights are based, possibly due to anomalously poor weather. The weights- and noise-rms-based cuts eliminate an additional 20 individual maps at 150 GHz and 29 individual maps at 220 GHz.

All observations of the RA5H30DEC-55 field that survive the data selection cuts were taken with the Sun below the horizon. The moon was above the horizon for 52% of these observations but was never closer than 80 deg from the field center. Cross-checks performed for power spectrum analyses using these data (Lueker et al. 2010; Shirokoff et al. 2011; Keisler et al. 2011) have shown no evidence of contamination from moon pick-up. The observations of the RA5H30DEC-55 field sample the full range of azimuth directions. Cross-checks performed for power spectrum analyses using these data (Lueker et al. 2010; Shirokoff et al. 2011; Keisler et al. 2011) have shown no evidence of contamination from ground-based signals on spatial scales that are measured in these maps.

After all of these checks and cuts, the final 150 GHz maps presented here are built from 321 individual observations totaling 621 hr, with a median number of 304 individual detectors contributing data during each observation. For the 220 GHz maps, 313 observations totaling 605 hr are included, with a median number of 166 detectors contributing data.

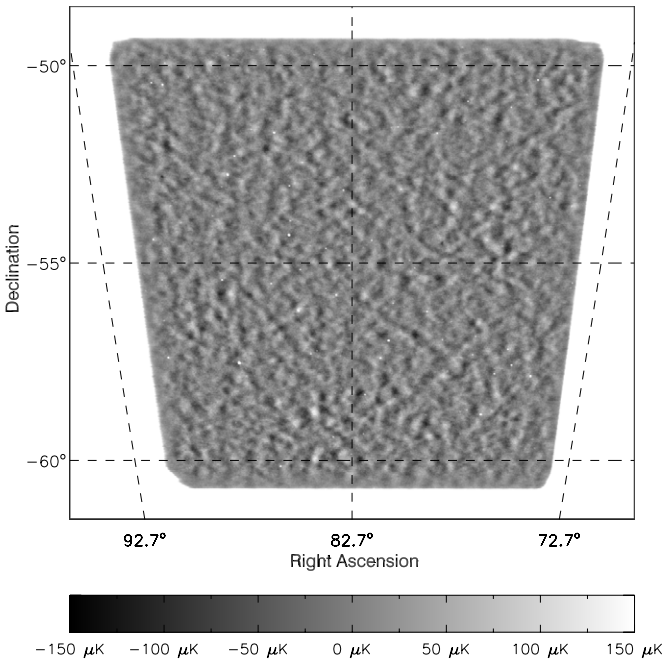

Figure 3. Map of the RA5H30DEC-55 field at 150 GHz, using point-source masking in the data filtering and employing the Sanson–Flamsteed projection. This is the filter and projection scheme tailored for performing cluster analysis. For display purposes, the map has been smoothed with a 1 arcmin FWHM Gaussian, and high-noise regions near the boundary of the map have been masked.

6. MAPS

6.1. Overview

SPT maps are constructed by a simple inverse-noise-weighted averaging of observations of a given map pixel. Noisy modes are filtered out of the timestream rather than de-weighted in the map-making, and the resulting map is not an unbiased estimate of the sky signal. An understanding of both the noise and the effect of filtering on signal is essential for interpreting the maps.

Ideally, the data processing and map projection would be optimized separately for different science goals. In order to present a relatively simple set of data products, we have selected two variations on filtering and projection choices. The first set of maps, created with cluster finding in mind, is produced using point-source masking in the TOD filtering, using the Sanson–Flamsteed projection. The second set of maps, created with point-source characterization in mind, is produced without masking bright sources in the filtering, using the oblique Lambert azimuthal equal-area projection.

The 150 GHz and 220 GHz maps with these processing and projection choices are presented in Figures 3–6. For display, each map has been smoothed by convolving it with a 1 arcmin FWHM Gaussian to suppress noise on scales smaller than the approximate size of the beam, and high-noise regions near the boundary of the map have been masked. Figure 7 shows one-dimensional (azimuthally averaged in ℓ space) signal+noise and noise PSDs for each map (computed from the point-source-masked maps in the Sanson–Flamsteed projection). These plots are included to illustrate: (1) where in spatial frequency the maps are signal- or noise-dominated; (2) where the noise is

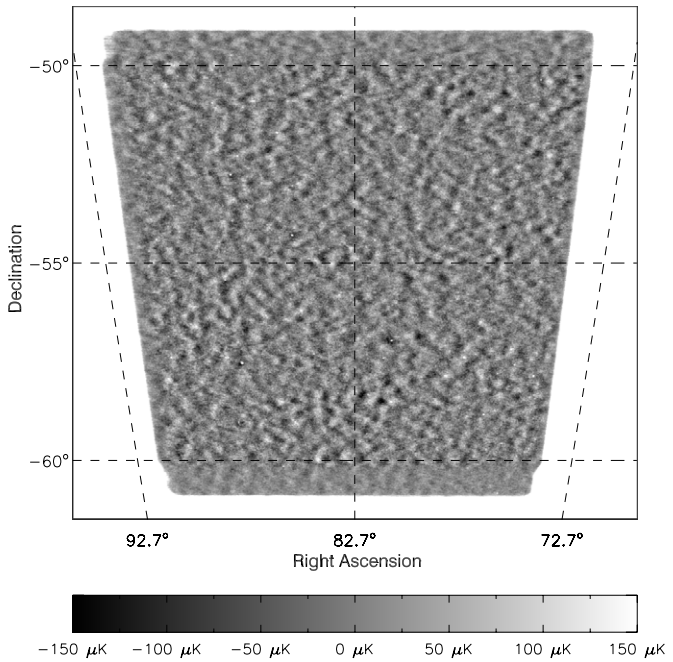

Figure 4. Map of the RA5H30DEC-55 field at 220 GHz, using point-source masking in the data filtering and employing the Sanson–Flamsteed projection. This is the filter and projection scheme tailored for performing cluster analysis. For display purposes, the map has been smoothed with a 1 arcmin FWHM Gaussian, and high-noise regions near the boundary of the map have been masked.

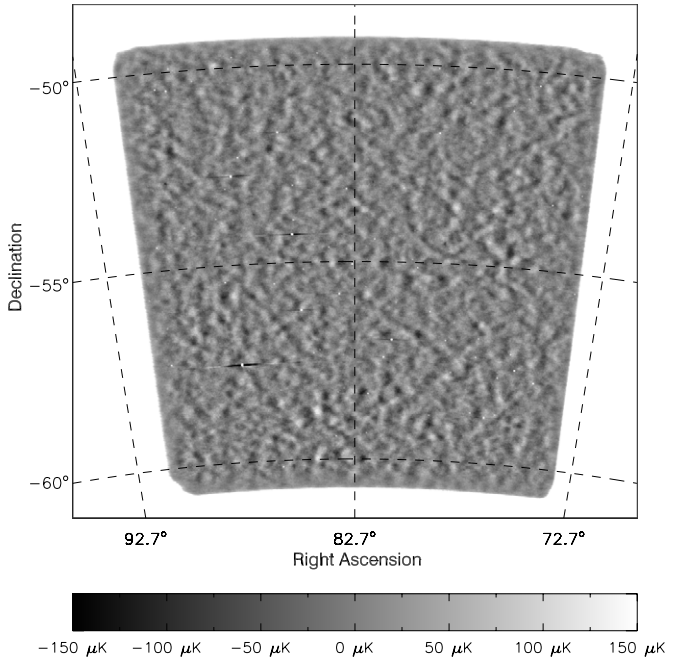

Figure 5. Map of the RA5H30DEC-55 field at 150 GHz, with point sources unmasked during data filtering, using the oblique Lambert equal-area azimuthal projection. This is the filter and projection scheme tailored for performing point-source analysis. For display purposes, the map has been smoothed with a 1 arcmin FWHM Gaussian, and high-noise regions near the boundary of the map have been masked.

white and where it has a "red" spectrum due to atmosphere; and (3) what signals are contributing at different spatial frequencies. In the following sections, we discuss estimates of the filtering and noise properties of the maps.

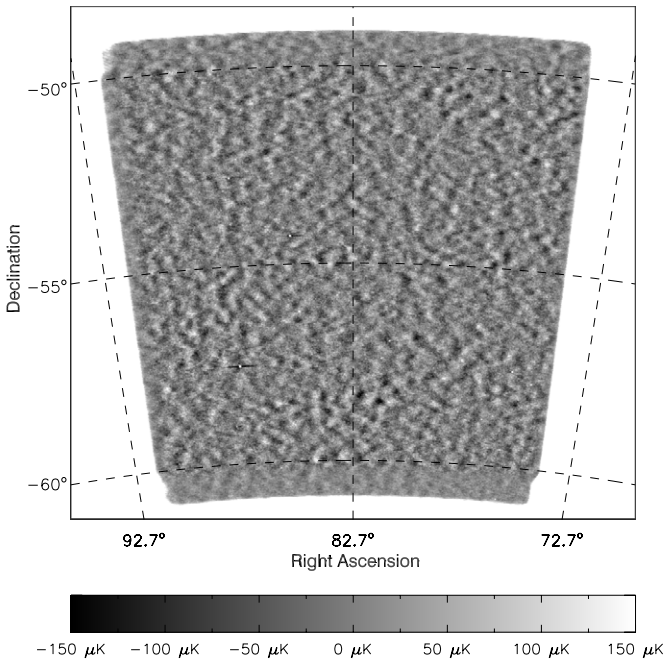

Figure 6. Map of the RA5H30DEC-55 field at 220 GHz, with point sources unmasked during data filtering, using the oblique Lambert equal-area azimuthal projection. This is the filter and projection scheme tailored for performing point-source analysis. For display purposes, the map has been smoothed with a 1 arcmin FWHM Gaussian, and high-noise regions near the boundary of the map have been masked.

6.2. Filter Transfer Functions

The beam and the timestream filtering are the two response functions that have the most impact on the properties of sky signals recorded in SPT maps. While these response functions are often combined, we separate them here because they vary in different ways with the choice of map projection. The beam functions were described in Section 4.4. In this section, we discuss how the time-domain filtering of the data from each scan combines to affect the properties of signals in the two-dimensional maps.

The data filtering, as discussed in Section 5.2, involves low-pass and high-pass filters with a wedge-average subtraction at each time sample. These TOD filtering operations combine with the coverage and projection to result in filtering of signal on certain spatial scales in the maps. We characterize the effect of filtering on sky signals by estimating the two-dimensional filter transfer functions. These are the Fourier-domain functions representing the relative suppression of signal power as a function of angular scale in the x and y dimensions of the map.

The transfer functions are typically estimated by simulating observations of a known signal using the reconstructed pointing for the real data, and passing the simulated observations through the full data analysis pipeline. Dividing the two-dimensional discrete FT of the simulated map by the FT of the input signal yields an estimate of the filter transfer function. Assuming that the effect of filtering is linear, the estimated transfer functions should be independent of the input signal used in the simulations. In practice, the estimated transfer function depends very slightly on the input signal used, but the difference averaged over all spatial modes of interest is less than 1%, even for input signals as drastically different as a point source and a simulated CMB sky. For the maps presented here, we have estimated the transfer functions using simulations of a Gaussian input signal with an

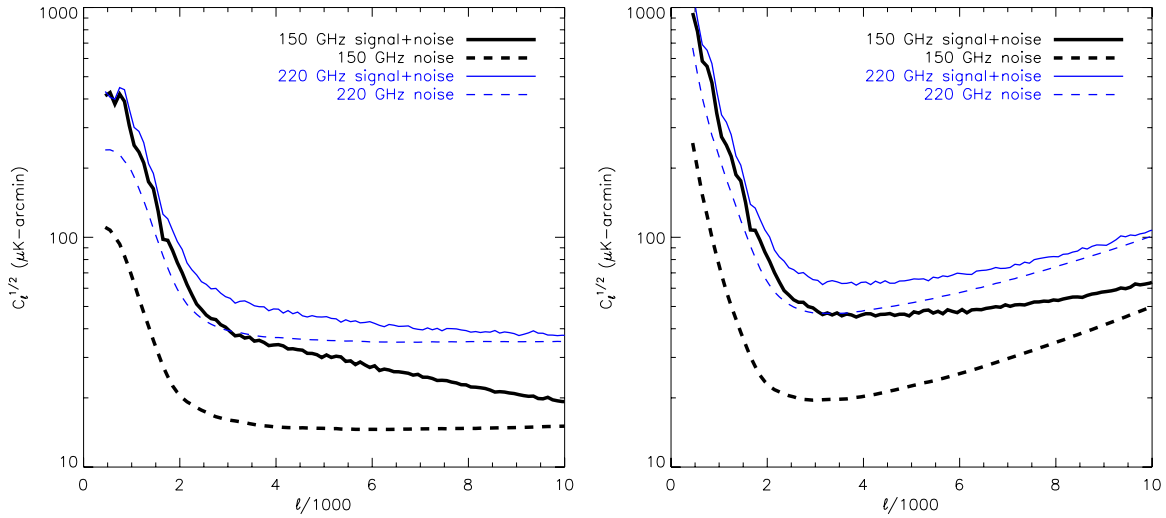

Figure 7. One-dimensional (azimuthally averaged in ℓ space) signal+noise and noise PSDs for each observing frequency. Left panel: signal+noise and noise-only PSDs from the raw map, uncorrected for beam and filtering effects. Right panel: as in left panel, but with the beam and filter transfer function divided out. Azimuthal averages are calculated using rough noise weighting, with noisier modes at low k_x (or ℓ_x) receiving less weight and modes below $k_x = \ell_x = 400$ ignored entirely. These demonstrate that the 150 GHz map is signal dominated at nearly all spatial frequencies out to $\ell = 10{,}000$, but that the 220 GHz map has significant noise contributions, particularly at $\ell \geqslant 5000$. The essentially white character of the map noise is evident above $\ell = 2000$ in the raw map PSDs. The signal+noise PSDs with the beam and transfer function divided out show that the damping tail of the primary CMB (steeply falling with ℓ) dominates the signal below $\ell \simeq 2500$, while the contribution from point sources (flat with ℓ) dominates above $\ell \simeq 2500$.

(A color version of this figure is available in the online journal.)

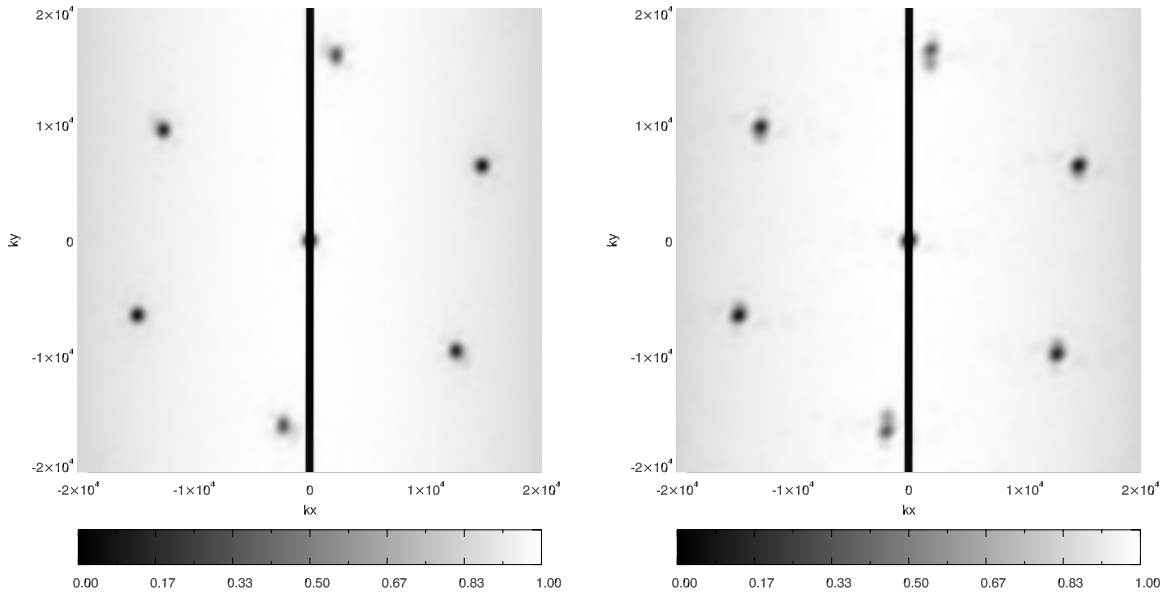

(a) Filter transfer function for 150 GHz (b) Filter transfer function for 220 GHz

Figure 8. Estimated two-dimensional transfer functions for the 150 GHz and 220 GHz maps employing point-source masking and the Sanson–Flamsteed projection. These are averages over the entire map. The dark stripe along $k_x = 0$ is due to the effective scan-direction high-pass filter from the polynomial and Fourier-mode subtraction, the dark spot centered at $k_y = k_x = 0$ comes from the isotropic high-pass filter of the wedge mean subtraction, and the hexagonally spaced dark spots are due to the sensitivity of the wedge mean subtraction to modes with wavelengths and angles corresponding to the detector array configuration. (See Sections 5.2 and 6.2 for details on filtering and associated transfer function features.)

FWHM of 0.75 arcmin, chosen to probe the spatial scales of interest in these maps.

Figure 8 shows the estimated two-dimensional filter transfer function for the maps tailored to cluster finding (filtered with point sources masked and presented with the Sanson–Flamsteed projection). In the Sanson–Flamsteed projection, the telescope scan direction is nearly equivalent to the x-direction in the map. This means that the low-pass and high-pass time-domain filters translate effectively into low-pass and high-pass spatial filters along the x-direction. The wedge-average filtering acts as a roughly isotropic high-pass filter. In addition, it produces localized decrements in the transfer functions at the spatial scales corresponding to the separation distances between individual detectors. Sky signal modes with wavelengths at the detection separation scale and aligned in angle with the pixel configuration will be almost perfectly removed by the wedge-average subtraction. The arrangement of these features reflects the hexagonal symmetry of the detector array. The angle between the

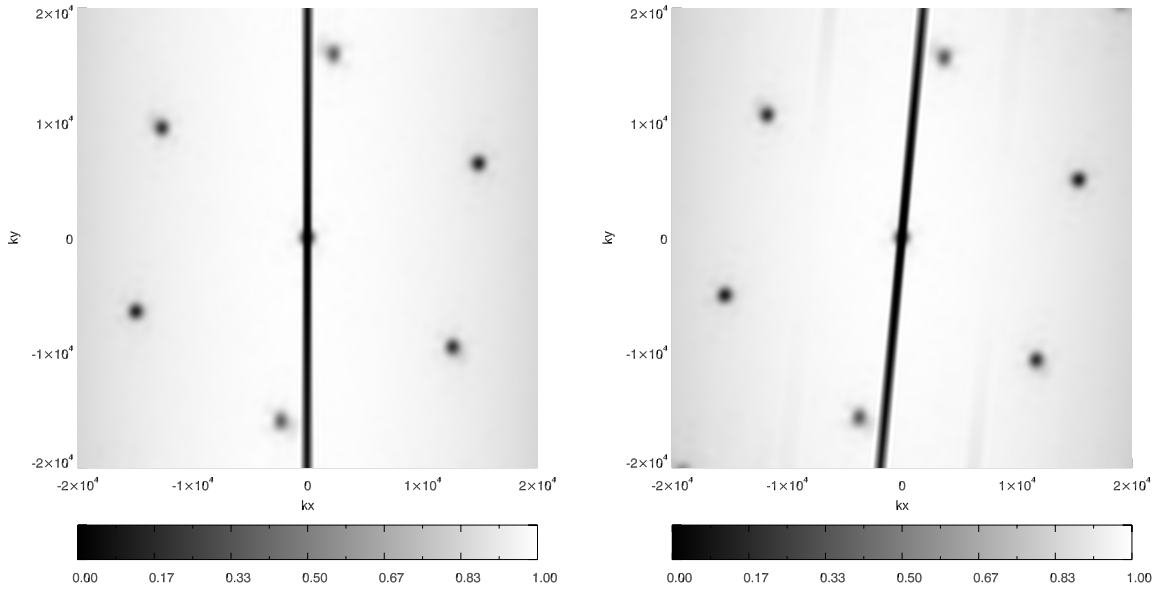

(a) Center filter transfer function for 150 GHz map

(b) Corner filter transfer function for 150 GHz map

(c) Center filter transfer function for 220 GHz map

(d) Corner filter transfer function for 220 GHz map

Figure 9. Estimated two-dimensional filter transfer functions for the 150 GHz and 220 GHz maps employing no point-source masking and the oblique Lambert equal-area azimuthal projection. The "center" filter transfer functions represent the innermost one-ninth of the map region, while the "corner" filter transfer functions represent one-ninth of the map region located in the lower right corner. See the caption to Figure 8 and Section 6.2 for a discussion of the obvious features in these transfer functions. The rotation of the features between center and corner transfer functions is discussed in Section 6.2.

symmetry axis of the features and $k_x = 0$ reflects the fact that the focal plane is slightly rotated with respect to the vertical axis of the telescope (to increase uniformity of map coverage along the elevation direction).

The width of the reconstructed map varies as a function of declination in the projection, so there is a slight change in the effective spatial cutoff scales for the high-pass and low-pass filters at the top and bottom of the map. Neglecting these small effects, the filtering is essentially uniform across the maps.

Filter transfer functions for the maps produced with the oblique Lambert equal-area azimuthal projection are more complicated. In this projection, the telescope scans are at an angle to the x-direction in the map, and this angle varies with position. This means that the two-dimensional transfer function rotates as a function of map position (the angle of rotation is equal to the angle between map rows and R.A., which is computed as a function of map position in Equation (6)). To address this rotation as well as more subtle changes with position, we have separately estimated the transfer functions with the input Gaussian signal placed in nine different locations in the map (the changes in transfer function across the map are sufficiently slow and regular that nine locations easily sample the full behavior). Figure 9 compares the estimated transfer function for the central portion of these maps to the estimated

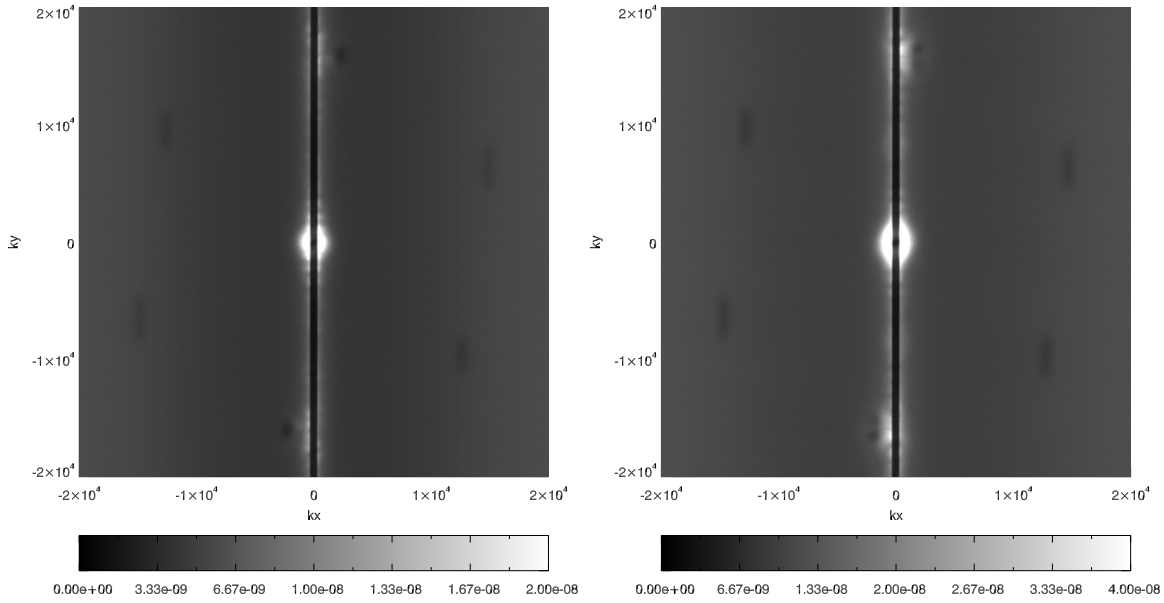

(a) Noise PSD for the 150 GHz map (b) Noise PSD for the 220 GHz map

Figure 10. Estimated two-dimensional noise PSDs for the 150 GHz and 220 GHz maps processed with point-source masking and the Sanson–Flamsteed projection. Note that these are averaged over the whole map area. The high-noise area near $k_y = k_x = 0$ is due to atmospheric noise, the uniformly increased noise at low k_x is due to low-temporal-frequency noise uncorrelated between detectors, and the areas of excess noise at $k_y \simeq 15{,}000$, $k_x \simeq 0$ are due to upmixed atmospheric power resulting from different sampling and filtering of atmospheric noise in different detectors' time-ordered data. As in the filter transfer functions (see Figures 8 and 9), the dark stripe along $k_x = 0$ is due to the effective scan-direction high-pass filter from the polynomial and Fourier-mode subtraction, and the hexagonally spaced dark spots are due to the sensitivity of the wedge mean subtraction to modes with wavelengths and angles corresponding to the detector array configuration.

transfer function in the lower right corner of the maps. The corner transfer function shows slight changes in the effective spatial scale of the low-pass filtering, and it exhibits additional diagonal features with amplitudes of 5%–10%. These features arise because the filtered power associated with a given bright source is spread diagonally across multiple rows of the map. In other words, they are a result of the interaction between the filtering and the sampling function associated with the map pixelization. For most applications, these features can be neglected, as long as the rotation is taken into account. The transfer functions for all nine sub-regions of the map are available online.

6.3. Map Noise

6.3.1. Map Noise Estimation and Description of Noise PSD Features

Each individual two-hour observation of the field yields a map with nearly identical sky signal contributions but independent atmospheric and instrumental noise. We estimate the two-dimensional noise PSDs for the final co-added maps using the jackknife noise estimation technique (Sayers et al. 2009; Halverson et al. 2009), which is used and described in many previous SPT publications (e.g., Staniszewski et al. 2009; Vanderlinde et al. 2010; Vieira et al. 2010). Here, we describe those functions, noting that we refer to the square root of the noise power spectral density function as the PSD.

Figure 10 shows the averaged two-dimensional noise PSDs estimated for the maps constructed with the Sanson–Flamsteed projection. For most of the signal region of interest for cluster finding and point-source characterization, the noise is essentially white. Because noise power in the TOD translates to slightly different spatial scales at the top and bottom of the map, there is an effective noise gradient of about 10%, scaling with the square root of the cosine of the declination in the map. The PSDs shown in Figure 10 and the depth values quoted in Section 6.3.2 are averages over all declinations in the map.

The most obvious non-white features in the PSDs are the concentration of high noise at low k (near the origin), the increase in noise toward low k_x, and the noise cutoff at k_x values below ∼300. The increasing noise at low k_x is due to $1/f$ noise that is uncorrelated between detector channels. The cutoff at low k_x is due to the high-pass filter, just as in the filter transfer functions in Section 6.2. High noise near the origin is due to brightness fluctuations in the atmosphere. These fluctuations are spatially isotropic and have a very "red" spectrum, with most of the power on large spatial scales. Depending on the scan speed of the instrument, in any given observation the atmosphere will either be imaged as if it were a stationary sky signal, in which case the atmosphere will appear as isotropic noise at low k, just as it does in the composite PSDs shown here, or it will blow past the array in the direction of the wind, in which case it will appear elongated in k-space along the wind direction in a single-observation PSD. Even in the latter case, changes in wind direction over the course of many observations will tend to make the atmospheric contribution essentially isotropic.

The visible decrements in the PSDs in Figure 10 correspond to the features previously described in the two-dimensional transfer functions. Residual atmospheric noise contributes excess noise at large spatial scales, but the majority of the atmospheric and instrumental noise is removed by the high-pass filter. A small amount of noise power "leaks" into the central high-pass-filtered region of the Fourier plane because of the subsequent application of the wedge-average filtering. The areas of excess noise at high k_y/low k_x are explained as "upmixed" large-scale noise power. This upmixing occurs because the sampling and filtering of large-scale atmospheric features is slightly different in the TOD of each individual detector.

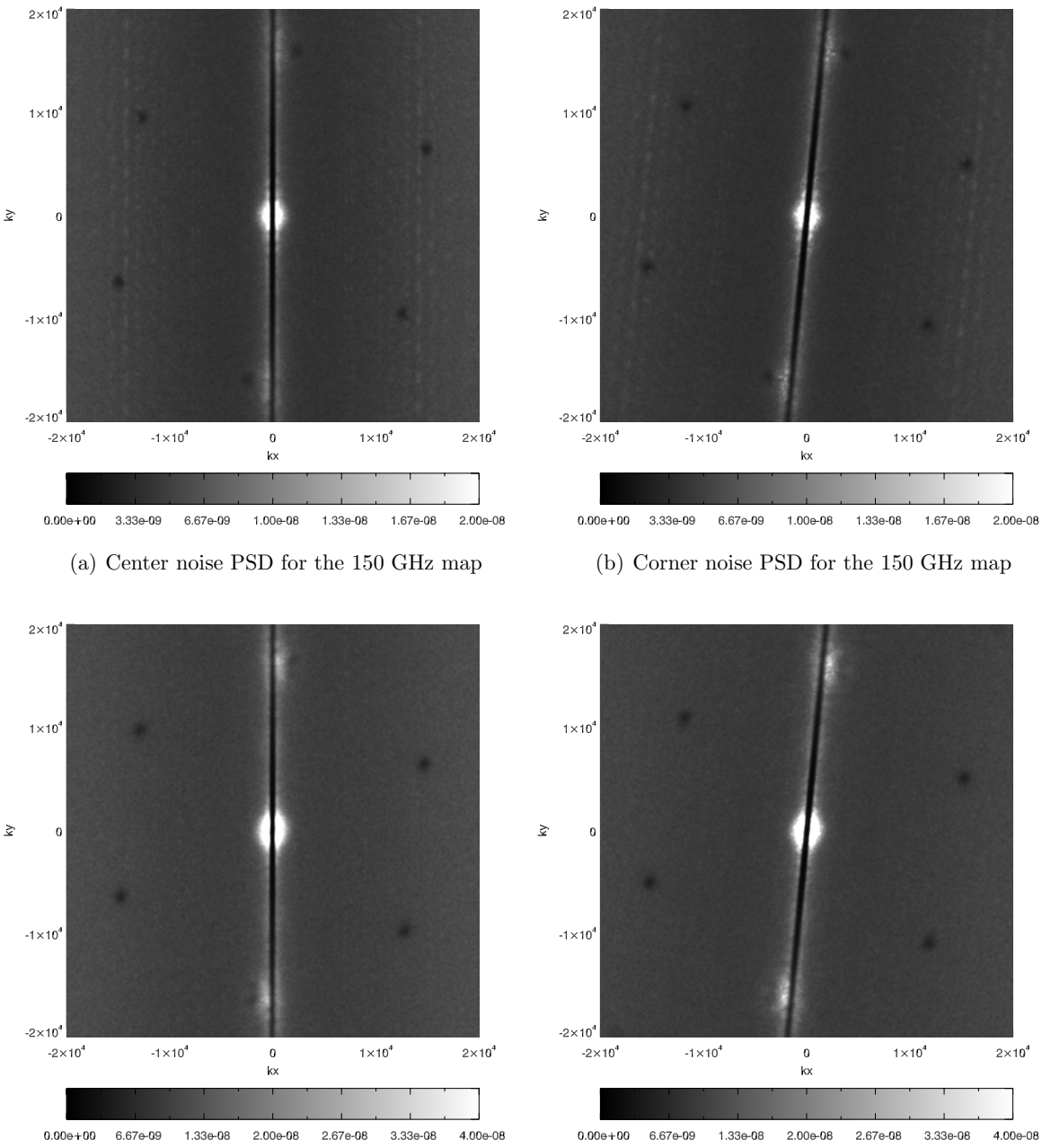

(a) Center noise PSD for the 150 GHz map

(b) Corner noise PSD for the 150 GHz map

(c) Center noise PSD for the 220 GHz map

(d) Corner noise PSD for the 220 GHz map

Figure 11. Estimated two-dimensional noise PSDs for selected sub-regions of the 150 GHz and 220 GHz maps processed with no point-source masking and the oblique Lambert equal-area azimuthal projection. The "center" PSDs represent the innermost one-ninth of the map region, while the "corner" PSDs represent one-ninth of the map region located in the lower right corner. See the caption to Figure 10 and Section 6.3.1 for a discussion of the obvious features in these PSDs. The faint lines at constant k_x (not apparent in the Figure 10 PSDs) are due to readout lines (see Section 6.3.1 for details). The rotation of the features between center and corner PSDs is discussed in Section 6.3.1.

Figure 11 shows the averaged two-dimensional noise PSDs estimated for the center and lower right corner of the maps with the oblique Lambert equal-area azimuthal projection. The properties are similar to those for the Sanson–Flamsteed projection, with the added rotation for positions away from the center of the map (the reason for this rotation and the value of the rotation angle are identical to those discussed for the filter transfer functions in Section 6.2). In these PSDs, the effect of residual high-frequency readout-related line features is visible as vertical strips at high k_x. These are less visible in the full-map average PSDs presented in Figure 10, but the features are present. These features have a negligible effect on analyses performed with the maps.

As with the transfer functions, PSDs have been estimated for nine sub-regions of the oblique Lambert equal-area azimuthal projection maps, and these data products are available to download.

6.3.2. Map Noise Accounting

The noise PSDs discussed in Section 6.3.1 can be used to estimate the effective map depths, but it is important to highlight that these numbers depend on the absolute calibration and on

the normalization of the beam functions. In previous SPT publications, map depth has been quoted under the approximation that the SPT beams are Gaussian, with $B(\ell) = 1$ at $\ell = 0$. Using the measured SPT beam presented here, with $B(\ell)$ normalized to unity at $\ell = 800$, the quoted map depth numbers are slightly different, but, as we will show, the two sets of beam/calibration/depth numbers are consistent with each other. Put another way, the fundamental quantity of interest for science is the noise after the beam and transfer function have been deconvolved, and the deconvolved noise we measure here is consistent with the Gaussian-beam estimates in previous papers, as shown below.

Quadrature-averaging an annulus of the PSDs between $\ell = 4000$ and $\ell = 5000$, we estimate a depth of 14.8 μK arcmin at 150 GHz and 36.1 μK arcmin at 220 GHz. For this estimate, as in Figure 7, azimuthal averages are calculated using rough noise weighting, with noisier modes at low k_x (or ℓ_x) receiving less weight and modes below $k_x = \ell_x = 400$ ignored entirely. This estimate of map depth must be interpreted using the beams reported in this release, because the calibration applied to the maps depends on the beam function shape and normalization.

For simple calculations of signal sensitivity, it is common to use a Gaussian approximation to the beam. If we approximate the beams as Gaussians with FWHM 1.15 arcmin and 1.05 arcmin for the 150 GHz and 220 GHz maps, respectively, we also need to modify the effective calibration of the maps. Within the ℓ range used for estimating the map depths, the average ratio of the true beam function to the Gaussian beam function can be used to adjust the depth figures. Over the ℓ range used in this noise estimate, that ratio is 0.86 at 150 GHz and 0.87 at 220 GHz. The depths appropriate for a Gaussian approximation to the beam are thus approximately 17 μK arcmin at 150 GHz and 41 μK arcmin at 220 GHz, as quoted in the abstract. These numbers are consistent with the quoted values of 18 μK arcmin and 40 μK arcmin from previous SPT publications (e.g., Vanderlinde et al. 2010; Shirokoff et al. 2011).

The 150 GHz beam-deconvolved noise at $\ell = 3000$ (see Figure 7, right panel) is 19.7 μK arcmin. This is equal to the beam-deconvolved noise amplitude at this multipole for a 1.15 arcmin FWHM Gaussian beam and 18 μK arcmin white noise. The 220 GHz beam-deconvolved noise at $\ell = 3000$ (see Figure 7, right panel) is 46.9 μK arcmin. This is equal to the beam-deconvolved noise at this multipole for a 1.05 arcmin FWHM Gaussian beam and 43 μK arcmin white noise.

In Section 2, we reported mapping speeds for the full detector array at 150 and 220 GHz, using the absolute temperature calibration described in this release. These numbers can be combined with the total integration time on the RA5H30DEC-55 field reported in Section 3 to obtain an estimate of the expected depth of the maps. A simple calculation using the numbers for mapping speed, field size, and integration time to determine depth would yield expected depths of roughly 11 and 29 μK arcmin at 150 and 220 GHz, respectively. These numbers are significantly lower than the 14.8 and 36.1 μK arcmin calculated directly from the noise PSDs. However, several factors reduce the time spent on the uniform-coverage region for which the field size of 95 deg^2 is reported. First, with a one-degree-wide detector array we must map an 11-by-11-degree region to end up with a 10-by-10-degree region which is seen by every bolometer. This results in an efficiency loss of roughly 20%. Second, the constant-velocity, bolometer, and scan cuts described in Section 5.1 result in an approximately 15% loss. When these cuts and inefficiencies are taken into account, the expected depths are 13.4 and 34.7 μK arcmin at 150 and 220 GHz, within 10% of the observed map depth. All map depth estimates assume that the noise is white, which is known to be only an approximation even for the ℓ range used for these estimates.

6.4. Comparison to Past SPT Analyses

The maps and data products presented in this release are very similar, but not identical, to maps of the RA5H30DEC-55 field used by the SPT team in previously published scientific results. These published results include catalogs of SZ-selected galaxy clusters (Staniszewski et al. 2009; Vanderlinde et al. 2010; Williamson et al. 2011) and emissive sources (Vieira et al. 2010), and measurements of the CMB angular power spectrum (Lueker et al. 2010; Shirokoff et al. 2011; Keisler et al. 2011). Minor variations in data selection, filtering, map projection, and approaches to defining transfer functions and noise PSDs are expected to cause small changes in catalogs of objects extracted from these maps and to estimates of the CMB power spectrum. We have reproduced two past catalogs and two past power spectrum analyses using this map release to verify that the differences are negligibly small.

Using the 150 GHz map from this release that was produced with the Sanson–Flamsteed projection and point-source masking, we have reproduced the analysis reported in Vanderlinde et al. (2010). All RA5H30DEC-55 clusters presented in Vanderlinde et al. (2010) (10 out of 21 total clusters in that work, which also included data from the RA23H30DEC-55 field) are clearly detected in our analysis with the data products from this release. The signal-to-noise values for these 10 clusters in our analysis agree with the values quoted in Vanderlinde et al. (2010) to within 2% in the mean, with an rms scatter of 4%. This check was performed using the estimated PSD presented in this release, but with the analytic transfer function estimate described in Vanderlinde et al. (2010). A cross-check using the simulated transfer functions and full two-dimensional beam functions presented in this release produces identical results at the sub-percent level.

Using both the 150 GHz and 220 GHz maps from this release that were produced with the oblique Lambert equal-area azimuthal projection and no point-source masking, we have reproduced the analysis reported in Vieira et al. (2010). This check was performed using the noise PSDs, transfer functions, and beams presented in this release. The Vieira et al. (2010) catalog is faithfully reproduced using the data products in this release, with every 5σ source from Vieira et al. (2010) detected at $\geqslant$4.4σ in our analysis and mean signal to noise within 0.1% of the Vieira et al. (2010) values at 150 GHz and 1.0% at 220 GHz. The recovered fluxes of the sources in this analysis compared to the Vieira et al. (2010) fluxes are 3.1% lower at 150 GHz and 7.5% lower at 220 GHz. These differences are due to improved beam and calibration estimates. If we repeat the analysis using the maps, filter transfer functions, and noise PSDs presented here and the beam and calibration used in the Vieira et al. (2010) analysis, we reproduce the 150 and 220 GHz flux numbers to better than 1%.

Finally, we construct a CMB power spectrum estimate from the 150 GHz data and compare it to the power spectrum of this field as measured in Shirokoff et al. (2011) and Keisler et al. (2011). In each comparison, we use the calibration used in the Shirokoff et al. (2011) or Keisler et al. (2011) analyses. We construct the power spectrum by Fourier transforming the

point-source-masked 150 GHz map times an adapted version of the apodization mask used in Shirokoff et al. (2011) or Keisler et al. (2011), correcting for the beam and transfer function, squaring, azimuthally averaging in ℓ space, and subtracting off a noise bias calculated by azimuthally averaging the squared noise PSD (also corrected for beam and transfer function). Fourier modes with significantly elevated noise or where the transfer function is near zero were excluded from the signal and noise averages.

We find that this simply calculated power spectrum of the ra5h30dec-55 map presented here, using the Shirokoff et al. (2011) calibration and masks, agrees with the power spectrum of this field from the Shirokoff et al. (2011) analysis to within 3% in power (1.5% in temperature). This small difference is attributable to mode-mixing and window-function effects that are not taken into account in the simple analysis performed here. We find that the power spectrum of the ra5h30dec-55 map presented here, calculated using the Keisler et al. (2011) calibration and masks, agrees with the power spectrum of this field from the Keisler et al. (2011) analysis to within 1% in power (0.5% in temperature).

7. CONCLUSIONS AND AVAILABLE DATA PRODUCTS

We have presented the first publicly released maps from the SPT, of a 95 deg^2 field observed during the 2008 season in two frequency bands (150 and 220 GHz). We have described the observations, data selection, filtering, and map-making approaches used to create these maps. In addition, we have characterized the instrument bands and beams, the filter transfer functions, and the noise properties of the maps. The maps and auxiliary data products documented in this paper are available online for download and use by the broader community. The full set of data products, available at http://pole.uchicago.edu/public/data/maps/ra5h30dec-55 and from the NASA Legacy Archive for Microwave Background Data Analysis server, includes the following.

1. *Maps*. Two versions of both the 150 GHz and 220 GHz maps of the ra5h30dec-55 field are given. One version uses the Sanson–Flamsteed projection and point-source masking in the filtering, and the other version uses the oblique Lambert equal-area azimuthal projection with no point-source masking.
2. *Beams*. Two-dimensional beam functions for 150 GHz and 220 GHz are provided, as well as one-dimensional beam averages in real and Fourier-space representations and an estimate of beam uncertainties.
3. *Bands*. Measured bandpass functions for 150 GHz and 220 GHz are provided.
4. *Filter transfer functions*. Two sets of transfer functions are provided, corresponding to the two choices of projection and filtering. For the oblique Lambert equal-area azimuthal projection, transfer functions estimated for nine sub-regions of the map are given.
5. *Noise PSDs*. Two sets of noise PSDs are provided, corresponding to the two choices of projection and filtering. For the oblique Lambert equal-area azimuthal projection, PSDs estimated for nine sub-regions of the map are given. An example of a calculation using these data products is described in the Appendix.

We have checked that these data products, when used in analyses similar to published analyses of this field's data, faithfully reproduce the published results. The data release and this accompanying paper are the first step toward an eventual release of data from the full 2500 deg^2, three-band SPT–SZ survey.

The South Pole Telescope is supported by the National Science Foundation through grants ANT-0638937 and ANT-0130612. Partial support is also provided by the NSF Physics Frontier Center grant PHY-0114422 to the Kavli Institute of Cosmological Physics at the University of Chicago, the Kavli Foundation, and the Gordon and Betty Moore Foundation. The McGill group acknowledges funding from the National Sciences and Engineering Research Council of Canada, Canada Research Chairs program, and the Canadian Institute for Advanced Research. Partial support at Harvard is provided by NSF grants AST-1009012, AST-1009649, and MRI-0723073. B.A.B. is supported by a KICP Fellowship. M.D. and N.H. acknowledge support from Alfred P. Sloan Research Fellowships. R.K. acknowledges support from NASA Hubble Fellowship grant HF-51275.01. J.J.M. acknowledges support from the DFG supported Excellence Cluster Universe and the transregio program TR33: Dark Universe. B.S. acknowledges partial support from the Brinson Foundation. We acknowledge the use of the Legacy Archive for Microwave Background Data Analysis (LAMBDA). Support for LAMBDA is provided by the NASA Office of Space Science.

APPENDIX

EXAMPLE CALCULATION

As a simple introduction to the use of the data products presented here, and as a means for users to check that they are interpreting the data as intended, we present an example of a typical calculation, namely, the estimation of the flux of a point source in the map.

The most straightforward way to estimate the flux of a point source with a known position is to read off the map value at the pixel that corresponds to that position, and to convert that value in K-CMB to a value in MJy sr^{-1} using the conversion factors in Table 1. To convert that to a point-source flux in Jy, one needs an effective solid angle. It is tempting to simply use the solid angle of the beam; however, that implicitly assumes that signals in the map have undergone no filtering beyond beam smoothing, which is not necessarily the case. In the case of a filtered map, the effective solid angle to use in this calculation is (e.g., Vieira et al. 2010)

$$\Delta\Omega = \left[\frac{1}{4\pi^2}\int d^2k\; B(k_x, k_y)\; F(k_x, k_y)\right]^{-1}, \qquad \text{(A1)}$$

where $B(k_x, k_y)$ is the two-dimensional Fourier-space beam function and $F(k_x, k_y)$ is the two-dimensional Fourier-space filter transfer function.

This calculation will give an unbiased estimate of the source flux, but the estimate will be noisier than it has to be, because all spatial modes are treated equally, regardless of noise. If the map is filtered further to downweight noisy modes, the signal-to-noise on objects with a known angular profile (such as point sources) can be improved. The Fourier-space optimal filter for sources of a known shape is (e.g., Haehnelt & Tegmark 1996)

$$\psi(k_x, k_y) \equiv \frac{\tau(k_x, k_y) N^{-1}(k_x, k_y)}{\sqrt{\tau^2(k_x, k_y) N^{-1}(k_x, k_y)}}, \qquad \text{(A2)}$$

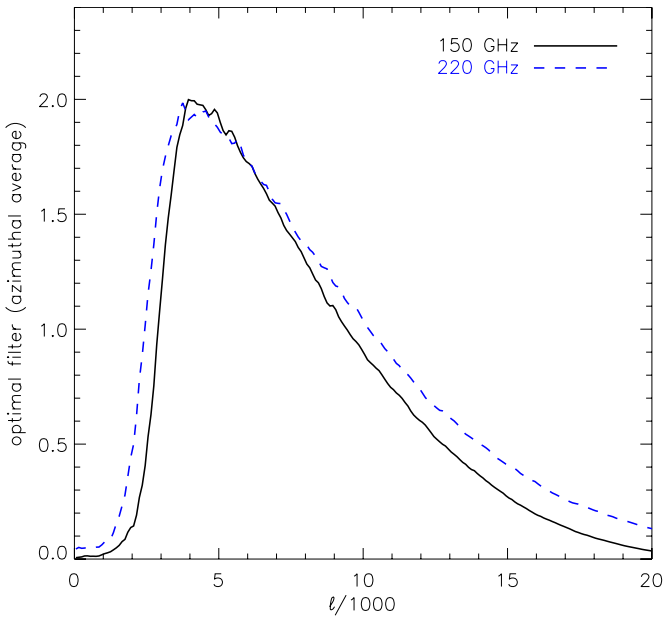

Figure 12. Azimuthally averaged optimal filters for point-source extraction, constructed using the data products in this work and the CMB power spectrum from Larson et al. (2011).

(A color version of this figure is available in the online journal.)

where τ is the (Fourier-space, beam-and-filtering-convolved) source profile, and N is the (Fourier-space) noise covariance matrix, which we assume to be diagonal. The noise covariance can include contributions from unwanted sky signals (convolved with the beam and filtering) as well as instrumental and atmospheric noise. For point sources, the source profile is entirely a function of the beam and filtering:

$$\tau_{\rm PS}(k_x, k_y) = B(k_x, k_y)\ F(k_x, k_y). \quad \text{(A3)}$$

To extract source fluxes from the optimally filtered map, the values at the pixel location should be multiplied by the conversion factor in Table 1 and an effective solid angle that now also includes the optimal filter ψ; however, if the filter is properly normalized as in Equation (A2), then the effective solid angle will not change.

We can now estimate the flux of a known source in the SPT map using the raw data and an optimally filtered map. The radio source PKS 0549-575 (also known as SPT-S 055009-5732.3) is located at R.A. 87°.5399, decl. −57°.5401, which corresponds to pixel location [937,928] (zero-based indexing) in the oblique Lambert equal-area azimuthal projection maps. The values in the point-source-unmasked 150 and 220 GHz maps at this pixel location are 10.084×10^{-3} and 8.508×10^{-3} K-CMB. Multiplying by the radio-source conversion factors in Table 1 yields values of 3.996 and 4.056 MJy sr^{-1}. Multiplying the Fourier-space beam by the filter transfer function appropriate to the source location in each band and integrating over all k values yields effective solid angles of 1.523×10^{-7} and 1.220×10^{-7} sr, leading to source flux estimates of 0.6086 and 0.4949 Jy. We can estimate the statistical uncertainty on these values by measuring the pixel variance in the neighborhood of this source and converting that number to Jy. This procedure yields rms uncertainties of 0.0043 and 0.0081 Jy at 150 and 220 GHz.

If we assume that the only signals in the map are CMB fluctuations and point sources, we can build an optimal filter using the source profile defined in Equation (A3) and a noise power spectrum that is the sum of the (squared) instrument-plus-atmosphere PSD and the CMB power spectrum. Because we have filtered the CMB, the version of the power spectrum that goes into the optimal filter must be multiplied by $[B(k_x, k_y)F(k_x, k_y)]^2$. Figure 12 shows the azimuthally averaged optimal filter at 150 and 220 GHz using the data products presented here and the CMB power spectrum from Larson et al. (2011). After convolving the maps with these filters, the map values at the location of PKS 0549-75 are 10.263×10^{-3} and 8.761×10^{-3} K-CMB at 150 and 220 GHz. As expected, the effective solid angle is the same as before application of the optimal filter, and the source flux estimates obtained by multiplying these optimally filtered map values by the radio-source conversion factors in Table 1 and the solid angles calculated above are 0.6194 and 0.5096 Jy. Estimating the flux uncertainties as we did with the unfiltered map yields rms uncertainties of 0.0016 and 0.0032 Jy at 150 and 220 GHz. For a source this bright, these statistical uncertainties are dwarfed by the calibration and beam uncertainties.

REFERENCES

Ade, P. A. R., Pisano, G., Tucker, C., & Weaver, S. 2006, Proc. SPIE, 6275, 62750U
Battaglia, N., Bond, J. R., Pfrommer, C., Sievers, J. L., & Sijacki, D. 2010, ApJ, 725, 91
Bussmann, R. S., Holzapfel, W. L., & Kuo, C. L. 2005, ApJ, 622, 1343
Calabretta, M. R., & Greisen, E. W. 2002, A&A, 395, 1077
Carlstrom, J. E., Ade, P. A. R., Aird, K. A., et al. 2011, PASP, 123, 568
Carlstrom, J. E., Holder, G. P., & Reese, E. D. 2002, ARA&A, 40, 643
Coble, K., Ade, P. A. R., Bock, J. J., et al. 2003, arXiv:astro-ph/0301599
De Zotti, G., Massardi, M., Negrello, M., & Wall, J. 2010, A&A Rev., 18, 1
Dicker, S. R., Mason, B. S., Korngut, P. M., et al. 2009, ApJ, 705, 226
Dunkley, J., Hlozek, R., Sievers, J., et al. 2011, ApJ, 739, 52
Haehnelt, M. G., & Tegmark, M. 1996, MNRAS, 279, 545
Hall, N. R., Keisler, R., Knox, L., et al. 2010, ApJ, 718, 632
Halverson, N. W., Lanting, T., Ade, P. A. R., et al. 2009, ApJ, 701, 42
Högbom, J. A. 1974, A&AS, 15, 417
Holland, W. S., Robson, E. I., Gear, W. K., et al. 1999, MNRAS, 303, 659
Keisler, R., Reichardt, C. L., Aird, K. A., et al. 2011, ApJ, in press (arXiv: 1105.3182)
Komatsu, E., Smith, K. M., Dunkley, J., et al. 2011, ApJS, 192, 18
Kuo, C. L., Ade, P. A. R., Bock, J. J., et al. 2007, ApJ, 664, 687
Lagache, G., Puget, J.-L., & Dole, H. 2005, ARA&A, 43, 727
Larson, D., Dunkley, J., Hinshaw, G., et al. 2011, ApJS, 192, 16
Lueker, M., Reichardt, C. L., Schaffer, K. K., et al. 2010, ApJ, 719, 1045
Mauch, T., Murphy, T., Buttery, H. J., et al. 2003, MNRAS, 342, 1117
Mortonson, M. J., & Hu, W. 2010, Phys. Rev. D, 81, 067302
Murphy, T., Sadler, E. M., Ekers, R. D., et al. 2010, MNRAS, 402, 2403
Negrello, M., Hopwood, R., De Zotti, G., et al. 2010, Science, 330, 800
Nozawa, S., Itoh, N., Kawana, Y., & Kohyama, Y. 2000, ApJ, 536, 31
Padin, S., Staniszewski, Z., Keisler, R., et al. 2008, Appl. Opt., 47, 4418
Puchalla, J. L., Caldwell, R., Cruz, K. L., et al. 2002, AJ, 123, 1978
Radford, S. J. E. 2011, arXiv:1107.5633
Ruhl, J., Ade, P. A. R., Carlstrom, J. E., et al. 2004, Proc. SPIE, 5498, 11
Sayers, J., Golwala, S. R., Rossinot, P., et al. 2009, ApJ, 690, 1597
Sehgal, N., Bode, P., Das, S., et al. 2010, ApJ, 709, 920
Shaw, L. D., Nagai, D., Bhattacharya, S., & Lau, E. T. 2010, ApJ, 725, 1452
Shirokoff, E., Reichardt, C. L., Shaw, L., et al. 2011, ApJ, 736, 61
Snyder, J. P. 1987, Map Projections—A Working Manual (Washington, DC: US Geological Survey)
Staniszewski, Z., Ade, P. A. R., Aird, K. A., et al. 2009, ApJ, 701, 32
Story, K., Aird, K. A., Andersson, K., et al. 2011, ApJ, 735, L36
Sunyaev, R. A., & Zel'dovich, Y. B. 1972, Comments Astrophys. Space Phys., 4, 173
Vanderlinde, K., Crawford, T. M., de Haan, T., et al. 2010, ApJ, 722, 1180
Vieira, J. D., Crawford, T. M., Switzer, E. R., et al. 2010, ApJ, 719, 763
Williamson, R., Benson, B. A., High, F. W., et al. 2011, ApJ, 738, 139
Zahn, O., Zaldarriaga, M., Hernquist, L., & McQuinn, M. 2005, ApJ, 630, 657